Technische
Universität
Braunschweig

Masterarbeit

Untersuchung eines akustisch optimierten synthetischen Turbulenzgenerators im Rahmen von eingebetteter wand-modellierter LES

Niels Formella
Matrikelnummer **xxx**

Eidesstattliche Erklärung

Hiermit erkläre ich, Niels Formella, geb. am **xx.xx.xxxx**, des Eides statt, die vorliegende Master -Arbeit selbstständig und ohne fremde Hilfe verfasst und keine anderen als die angegebenen Hilfsmittel verwendet zu haben.

Göttingen, 10.6.2024

Acknowledgements

I would like to express my appreciation to my thesis supervisor Dr. Axel Probst and Dr. Roland Ewert for their invaluable patience and feedback throughout this project. Without their generous sharing of their knowledge and expertise this thesis would not have been possible. The opportunity to conduct this work at DLR has been a real honor. Additionally, I am also grateful to other group members at DLR for all the feedback sessions, tips, editing help, and moral support during this project. Lastly, I would like to mention my family, especially my parents, and friends and thank them for their belief in me throughout this process.

Contents

Nomenclature

Abbreviations

BFS	Backward Facing Step
C_f	Skin Friction Coefficient
CAA	Computational Aeroacoustics
CFD	Computational Fluid Dynamics
DDES	Delayed Detached Eddy Simulation
DES	Delayed Eddy Simulation
DNS	Direct Numerical Simulation
FRPM	Fast Random Particle Mesh
HRLM	Hybrid RANS-LES Methods
IDDES	Improved Delayed Detached Eddy Simulation
LES	Large Eddy Simulations
NS	Navier Stokes
RANS	Reynolds-averaged Navier-Stokes
RE	Reynolds-number
SA	Spalart-Almaras model
SI-units	Standard International Units
SRS	Menter's Shear Stress Transport
STG	Synthetic Turbulence Generation
TKE	Turbulence Kinetic Energy
WMLES	Wall-modeled Large-eddy Simulation

Chapter 1

Introduction

Scaling-resolving simulation (SRS) approaches, specifically hybrid RANS-LES methods (HRLM), are in many cases the only viable option to obtain flow predictions away from calibration conditions, for example, close to the borders of the design envelope of an aircraft. SRS approaches are also needed for noise prediction because its generation is the result of unsteady pressure fluctuations. One promising approach of HRLM is wall-modeled LES (WMLES) which aims at high accuracy while at the same time keeping the computational cost reasonably low. Even though WMLES can be used without injection of artificial turbulence, for example in cases with strong natural instabilities, for stable flows the transition from RANS to (embedded) WMLES must be promoted by the addition of outside turbulence. Key to embedded WMLES's success is not only the injection of turbulent content in parts of the flow but also the injected turbulence's realism. The Fast Random Particle Mesh method (FRPM) is a promising tool for providing such realistic content in form of synthetic turbulence. One of its potential advantages, among others, is that it may not be hampered by issues such as nonphysical pressure fluctuations commonly seen in turbulence generators which can negatively affect the aeroacoustic, and perhaps to a lesser extent the aerodynamic, solution [12]. This is due to FRPM's primary design for aeroacoustic application, besides generally promising a high level of realism in its unsteady turbulence modeling. However, to reach its full potential anisotropy must also be modeled. In the current project anisotropy was not specifically modeled as part of the synthetic turbulence.

In aerodynamics it is sufficient to predict the time-averaged (mean) flow quantities such as a vehicle's drag or lift. Turbulence models for the Reynolds averaged Navier-Stokes (RANS) do exactly that. They are also computationally affordable. Their downside is that they rely heavily on assumptions and empirical information. For turbulent "border" flows, away from calibration conditions, RANS models may fail to give accurate predictions. Examples are flows with massively separated regions. In recent years there has not been a major breakthrough in RANS modeling and a model that gives accurate results over the entire spectrum of turbulent flows seems currently out of reach [15]. RANS models, such as the Spalart-Almaras model (SA), have been around for decades and remain an industrial workhorse, especially in cases for which it is highly optimized, e.g., attached boundary layer flows. However, there is still the difficulty of representing the turbulent transport of momentum by Reynolds stresses, which basically means inability to capture the effect of organized turbulent structures into single-point averages of fluctuating velocity. More knowledge about organized turbulent structures has been gained but it remains challenging to transfer this to improved turbulence modeling [7].

SRS methods can deliver accurate flow predictions for a wide range of turbulent flows, only limited by what is computationally manageable. A direct numerical simulation (DNS) with the full Navier Stokes (NS) equations comes at such high computational cost that it is mostly limited to incompressible flows, low Reynolds numbers and simple geometries. More practical relevance

can be expected from large eddy simulations (LES). Here, the NS equations are only solved for the larger turbulent structures that can be resolved on the computational grid. Smaller structures are modeled. This enables accurate flow predictions for higher Reynolds numbers and more complex geometries than is the case for DNS but is still restricted in its practical application [7]. However, the root problem for SRS methods being so computationally demanding does not result from the complexity of the equations being solved. For example, the set of RANS model equations with the closure terms is certainly more complex to solve than the local full NS equations. Rather, the reason SRS methods are so computationally demanding is the necessity of a higher resolution time step and finer mesh to resolve the smaller turbulent temporal and spatial scales. For a RANS simulation a much coarser grid, i.e., fewer grid points, can be used than for a DNS of the same flow. This is precisely the advantage that a delayed eddy simulation (DES) or WMLES has over a pure LES, although the set of equations become more complex and prone to errors, also in their implementation. On the other hand, an advantage of utilizing less modeling is less dependence on empirical information and being closer to the actual physical equations which allows more accurate results away from calibration conditions.

The idea of HRLM is to use SRS in terms of LES wherever it makes sense computationally while using RANS modeling only in limited parts of the flow where it is known to perform well, such as attached boundary layers. This gives rise to the idea of using a detached eddy simulation (DES) to limit the LES flow regime to the separated shear layer because it is what determines the major aerodynamic characteristics, while the attached boundary layer only plays a minor role and can be well modeled with RANS [12]. DES is a zonal approach because the RANS and LES zones are not specified in advance by the user, instead they are automatically determined during runtime. In the original DES formulation switching between RANS and LES mode is entirely dependent on the local mesh resolution [14]. This, however, can cause problems when switching from RANS to LES because the LES needs resolved turbulent content to properly function and the upstream RANS model cannot provide it. Proper RANS modeling is also not possible as the eddy viscosity is too low due to the smaller LES length scale applied in this region. That is why it is referred to as the grey area, an area of unclear modeling between RANS and LES. The delayed detached eddy simulation (DDES) and the improved delayed detached eddy simulation (IDDES) are improved versions of DES, addressing the grey area problem as well as other known issues such as the stress depletion and the log layer mismatch [13] [8]. The idea is to have the RANS and LES zones not only determined by the local mesh resolution but also to introduce the actual solution into the equation. Then a hybrid length scale is defined which takes on a functional dependency that is well suited for each zone while smoothly blending the length scales between them. In the case of IDDES the transition from one length scale to another can be rather fast. This is one of the reasons it can be utilized in one of its modes, namely WMLES. Detection of the different zones happens through a function which is both based on the local mesh resolution and the presence of turbulent content [11].

In the classical DES use case of a massively separated flow, e.g., behind a step or landing gear, the noise production is mainly due to the turbulent structures in the separated shear layer and recirculating area. Therefore, DES-like methods have found application in noise generation studies. This is different, however, for only mildly separated flows and attached boundary layers. In that case, the noise is produced by the turbulent vortical structures inside those relatively stable flows. The difficulty is that these flows lack the natural instabilities occurring in massively separated regions, such as behind the backward facing step (BFS) or cove of a multi-element wing. This is where non-zonal methods are known to have deficiencies in their accuracy, e.g., the grey area problem, while a full LES is computationally too costly for realistic (high) Reynolds-number (RE) flows. To reduce the cost, zonal approaches with a priori definition of the RANS and LES regions are the only viable option in terms of accurate aerodynamic and aeroacoustic predictions. Further advantage can be gained in WMLES where RANS modeling is used in proximity to the wall, while the larger turbulent structures farther away from the wall are resolved with

LES. This goes in hand with the previously discussed idea of saving grid points by an increase of modeling, where in WMLES the near wall RANS serves as a wall model, while the larger turbulent structures farther from the wall can be resolved by the LES on the computational grid.

A complicating factor in embedded WMLES from a user's perspective is the requirement for artificial turbulence injection into the flow field upstream of the location of interest. Without this injection and lack of natural instabilities in a stable attached boundary layer, the LES region lacks turbulent content which is known to damage the solution because it takes too far for mature turbulence to develop downstream of the zonal RANS region [12]. As it is of highest priority to shorten this adaption region, the injection of high quality artificial turbulence is needed. Several approaches exist, such as:

- Precursor DNS or LES

- Recycling of turbulence

- Synthetic turbulence generation

- Artificial forcing

- Vortex generating devices

Detailed descriptions can be found in [12]. All artificial turbulence injection methods seek to introduce realistic velocity fluctuations into the flow field. Only then can the adaption length be reduced to only a few boundary layer thicknesses downstream of the turbulence injection. If the artificial turbulence does not conform to the actual physics, i.e., the underlying NS equations, or in this case WMLES equations, then the turbulence is likely to be annihilated within a short distance of its injection. An analogy would be a person with an artificial heart. For it to be accepted by the human body it must blend in and be as real as possible. Otherwise it is rejected and cannot continue to do its job of keeping the system going. In the case of injected turbulence in embedded WMLES, without resolved turbulence the adaption length is too long and the solution is damaged. Therefore, different synthetic turbulence injection methods have been investigated for the DLR-TAU solver by Probst et al. [10].

In this thesis, the focus is on the synthetic turbulence generator FRPM which promises to create high fidelity turbulent fluctuations that reconstruct the turbulence statistics of the Menter-SST (SST) k-ω RANS model, based on its length and time scales [4]. Good agreement was shown in terms of noise prediction and matching of the SST turbulence kinetic energy [2]. The former is particularly promising since one major drawback of currently available synthetic turbulence generators is the production of unwanted and nonphysical spurious noise that shows up as unrealistically high pressure fluctuations in the solution. The reason for these pressure peaks is the sudden appearance of highly energetic vortical structures just downstream of the RANS-LES interface. Often the instantaneous continuity equation is disobeyed. Therefore, pressure peaks should be avoided to also prevent the aerodynamic solution from being impacted. This is a field of extensive research and the aeroacoustically optimized FRPM turbulence generator was specifically designed to behave well in this regard so that it qualifies to be tested in an aerodynamic setup.

In [2] FRPM is coupled with the DLR CAA solver PIANO using the so-called eddy-relaxation term. Therefore, the same method is applied in this project for the coupling of FRPM with the DLR CFD solver TAU. It is then investigated in terms of its strengths and weaknesses for WMLES applications. One of the indicators for good aerodynamic performance is an accurate prediction of the skin friction as wrong predictions can prevent correct estimates of the performance, e.g., of an aircraft. An underpredicition of the skin friction, however, is commonly seen with these methods [13]. Therefore, it is one of the main investigations in the results to come.

In this thesis, after a brief theoretical section in chapter 2, the meshes and numerical settings

in the two applied test cases, the flat plate and backward facing step (BFS), are described
in chapter 3. These test cases were chosen due to differences in the amount of intrinsic flow
instabilities, with weak and strong instabilities, respectively. Then in chapter 4 the setup of
the turbulence generator FRPM and FRPM standalone results without coupling to DLR-TAU
are presented. In chapter 5 results of TAU coupling with FRPM are described, beginning with
investigations using the flat plate case in Section 5.1. These results include a sensitivity study
describing the initial setup, followed by influence of changes in the initial setup by altering
the integral length scales, and thereby the size of the turbulent structures, variations in the
coupling parameter σ, addition of Langevin time de-correlation, and the effect of the FRPM
patch length. In particular, effects of the variations on deviations in the skin friction coefficient
C_f and particularly shortening the adaption region are considered, as well as influence on the
production of unwanted noise due to pressure fluctuations. Results for FRPM-TAU for the BFS
case are then described in Section 5.2 To conclude this chapter, in Section 5.3 an aerodynamic
test case is presented. Overall conclusions and outlook are presented in Chapter 6.

Chapter 2

Theory: A brief overview

This chapter briefly gives some theoretical background about the underlying methods in the following chapters.

2.1 WMLES

WMLES was already motivated and described in chapter 1. Here, it is just briefly added how the different modes in IDDES are detected, i.e., the WMLES branch and DDES branch. There is a mesh dependent part and a solution dependent part and reads as follows:

$$
r_d = \frac{v_t + v}{\kappa^2 d_w^2 \max\left(\sqrt{\frac{\partial U_i}{\partial x_j}\frac{\partial U_i}{\partial x_j}}; 10^{-10}\right)}
\tag{2.1}
$$

,

where the square root term in the denominator is the solution depended part. Actually, it is a little more detailed than this and the reader is referred to [11] for more detailed information. The hybrid length scale varies as

$$
l_{\text{hyb}} = \tilde{f}_{\text{d}}\left(1 + f_{\text{e}}\right) l_{\text{RANS}} + \left(1 - \tilde{f}_{\text{d}}\right) l_{\text{LES}}
\tag{2.2}
$$

In this project the WMLES mode was manually enforced.

2.2 STG

The STG by Adamian is compared to the BFS in section 5.4.2. Here, a fixed number of spatiotemporal Fourier modes is superimposed. As opposed to FRPM, the target are the Reynolds stresses and not the TKE. Therefore, the turbulent shear stress is directly enforced. For detailed information the reader is referred to [1] or to Probst et al. [10].

2.3 FRPM

In FRPM, particles of random numbers are convected through the domain following streamlines. Through spatial convolution of the white noise field with a Gaussian filter kernel, fluctuating quantities are obtained. Several source terms exist, e.g., fluctuating velocity or a divergence-free vorticity fluctuations field. Vorticity fluctuations were available in this investigation, which leads

to the method for injecting the vorticity fluctuations, namely the eddy-relaxation term in the next section.

2.4   Eddy-relaxation term

The eddy-relaxation term is discussed in detail in [5] and is defined as follows,

$$\sigma \left(\Omega'_k - \Omega_k^{\text{ref}} \right) \tag{2.3}$$

,

where Ω'_k are the resolved vorticity fluctuations and Ω_k^{ref} . σ is of the order of the eddy viscosity [2]. This term is similar to a viscous stress term and this is how the synthetic turbulence is injected into the governing equations since FRPM provides vorticity fluctuations and not velocity fluctuations as in the equations of the SA-WMLES setup in this investigation. Its effect on the turbulence injection is thoroughly discussed in section 5.1.2.

Chapter 3

Test cases and numerical setup

In this chapter the test cases and numerical setup are described. Specifically, the meshes, synthetic turbulence setup and underlying numerical settings are discussed.

3.1 Test cases

The test cases investigated in chapters 5 and 5.2 are presented in subsections 3.1.1 and 3.1.2, namely the flat plate and BFS. This chapter focuses on the TAU part and the used HRLES meshes.

3.1.1 Flat plate

A spatially developing turbulent attached boundary layer flow with zero pressure gradient and zero BL thickness at the start is investigated.

The hybrid mesh of Probst et al. [10] is used. In total it consists of $5.8 \cdot 10^6$ points and ensures $\Delta x^+ \approx 100 - 200$, $\Delta y^+ \approx 1$ and $\Delta z^+ \approx 50$. Standard practice was adhered to and mesh cells gradually stretched for $x/\delta_0 > 77$ to gradually dampen the turbulent fluctuations and ensure that the region is free of wave reflections. A physical time step of $8 \cdot 10^7 s$ was used.

The flow conditions were as follows:

freestream velocity U	70 m/s
static pressure	99120 Pa
Temperature	287 K
Reynolds number	$4.72 \cdot 10^6/m$
Mach number	$M_0 = 0.2$

The location of the RANS-WMLES interface is at $x = 0.3517m$ with $\delta_0 = 0.0058$ and a Reynolds number of $R_{e\theta} = 3040$.

3.1.2 Backward facing step

The BFS is a typical test case for HRLM because of its separated shear layer and recirculating flow region behind the step which leads to natural instabilities. The mesh in this project is a modification of the hybrid mesh in [6], while the latter is also compared to it in the coupling of FRPM and TAU. The difference in the meshes is that in the turbulence injection region the modified version has a finer and equidistant grid spacing of $\Delta x = 1/10\delta_0$ in the streamwise direction and $\Delta z = 1/20\delta_0$ in the spanwise direction. The wall normal spacing is unchanged. Except near the injection region the mesh is unaltered from [6].
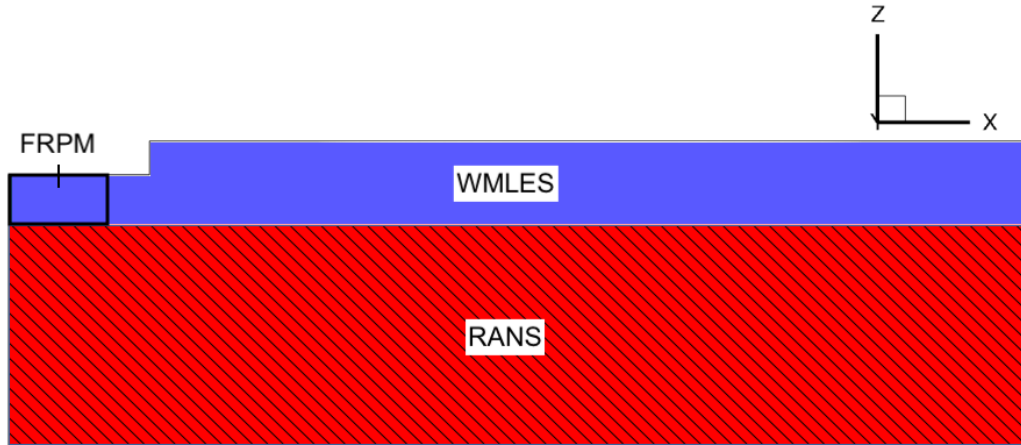
Figure 3.1: The setup for the BFS is shown.

The RANS and WMLES regions are shown in fig. 3.1 with the synthetic turbulence injection region being placed half a cell length from the inflow.

The inflow conditions are a inflow felocity of U=44.2 m/s and a Reynolds number (step height) of 37000.

3.1.3   DLR F15

The F15 mesh is the same as in [16].

3.2   Numerical setup

The solutions in the following sections were obtained using the German Aerospace Agency compressible solver DLR-TAU. It is particularly designed to work on unstructured meshes using a finite-volume discretization. The spatial and temporal discretization schemes are of 2nd-order. For incompressible flows, low-Mach number preconditioning is applied. In the following investigations the LD2 scheme, a low dissipation and dispersion scheme, is used for the inviscid fluxes as this delivers good results for scale-resolving simulations [9].

The SA-RANS model is used in conjunction with LES in a HRLES setup, whereby a WMLES branch of IDDES is specifically employed downstream of the zonal RANS region. Hence, the SA-model is not only acting upstream of the LES region but also in close proximity to the wall. The LES is acting outside of this near wall RANS region, where the turbulent structures are large enough to be resolved on the computational grid.

FRPM provides the turbulent content needed for the LES region to properly work and is then compared to the volumetric forcing STG proposed by Adamian et al. [1] in section 5.4.2. The latter works by superimposing a fixed number N of spatio-temporal Fourier modes and uses the Reynolds stresses as a target for its velocity fluctuations. It is also placed at the RANS WMLES interface and the forcing occurs over a length of $0.5\delta_0$ with the target stresses obtained at the RANS WMLES interface location.

Chapter 4

FRPM standalone

In this chapter the setup and results of using FRPM in standalone mode are presented. Standalone mode refers to only looking at the synthetically generated turbulence without any involvement of the DLR TAU-solver. The goal is to evaluate the quality of the synthetically generated turbulence and find a parameter set that is suitable for each test case.

4.1 FRPM setup

In these investigations the FRPM patch was set up to use SI-units. This facilitates its integration with TAU because the time step size, for example, is the same as the unsteady physical time step in TAU. No further error-prone conversion is needed. This is different from the non-dimensional units in the FRPM manual, but what is most suitable may vary depending on the CFD/CAA-solver FRPM is coupled with. A precursor SST solution can then be directly interpolated onto the FRPM patch, which involves quantities such as the turbulence kinetic energy (TKE) and dissipation rate ω. From these two quantities the length scale and a time scale can be calculated, as will be demonstrated in the following subsections.

Sections 4.1.1, 4.1.2, 4.1.3 describe parameters directly determined by the FRPM mesh or TAU settings, if not left completely unchanged as was the case with the filter type. The FRPM mesh, on the other hand, was carefully considered following the discussion in section 4.1.5. Closely related to the chosen mesh is the integral length scale which needs to be adapted accordingly and is investigated in section 4.2. The basic parameters for its manipulation are described in section 4.1.4.

4.1.1 FRPM time step

The time step was set to the unsteady physical time step size in the TAU-solver. It is limited in its maximum size by the FRPM mesh in the sense that a particle should not move further than a single cell per step. This has to do with how the FRPM code works internally and its ability to properly track the particle.

4.1.2 Number of particles

As for the number of particles, 4 times the number of grid nodes was used. This number should suffice while not risking having too few particles. For the flat plate FRPM patch this means $4 \cdot 92x60x24 = 132480$ particles. Only half as many particles may already be sufficient but the number of particles was chosen generously and no extensive study was carried out.

4.1.3   Filter type

A simple Gaussian filter was used. Its filter width correlates to the length scale obtained from the SST model.

4.1.4   Length scale parameters

$Lfac$ is a constant factor and scales the length scale. Multiplying this with l_{CFD} gives the integral length scale that correlates with the filter half width used in the internal FRPM filtering. Thus, $lfac \cdot l_{CFD,min}$ correlates with the size of the smallest turbulent structures while $lfac \cdot l_{CFD,max}$ sets an upper limit and $lfac$ scales the size of the turbulent structures in general.

l_{CFD} is needed to be calculated from the precursor SST solution and must be provided on the FRPM patch. It is calculated as $(TKE)^2/\omega$.

4.1.5   FRPM mesh

The mesh resolution used for the FRPM patch is closely tied to the filter type and length scale. This is due to the filtering between the grid points, where the filter width is linked to the integral length scale. A smaller length scale corresponds to a smaller filter width. Resolving the smallest turbulent structures, hence smaller length scales, requires a finer mesh. Thus, there is a trade-off between computational cost and the extent to which the smaller scales can be resolved by FRPM. This needs to be considered in close proximity to a surface, as this is where the length scales become small quickly due to the constraint imposed by the wall.

The FRPM mesh is generated in Tecplot by creating a rectangular zone which results in an orthogonal and equidistant grid. Curve-linear coordinates are not supported in the investigated version of FRPM [3].

A theoretical approach to finding a proper FRPM patch resolution is calculating the length scale from the Menter SST solution $l_{CFD} = \sqrt{k}/\omega$ and, according to the FRPM manual [3], adding a factor of 6 for isotropic turbulence. Then, the minimum length scale $l_{min,FRPM} = 6 \cdot \sqrt{k}/\omega$ in the injection region can be determined. A certain minimal number of cells are required to resolve this minimum length scale. Three to four cells can be a rough estimate. Depending on how fast the length scale decreases towards the wall, near wall artifacts can occur, as seen in section 4.2.

Taking this approach it becomes clear that an unpractically fine grid would be required to fully resolve the smallest turbulent structures. Further, the structures would become less realistic since FRPM generates isotropic turbulent structures, while the real world turbulent structures become increasingly anisotropic as the wall is approached. An idea better suited for WMLES could be to only allow FRPM to generate structures down to the length scale at the near-wall RANS/LES-interface, taking advantage of the RANS modelling close to the wall. Here, values are $l_{CFD} \approx 0.000052$ and $l_{min,FRPM} = 6 \cdot l_{CFD} = 0.000312$. With three cells for this length scale a grid spacing of a little over $ds = 0.000104$ is required in all directions. This is still a very fine mesh. Comparing this to the flat plate TAU mesh presented in section 3.1.1, it is realized that the FRPM patch would be 1/6th as fine in the streamwise direction and 1/3rd as fine in the spanwise direction. This does not yield any benefit because the TAU mesh would not be able to resolve these small scales and the Nyquist criterion would also set a limit. Therefore, a more practical approach should be taken, especially considering that the RANS/LES-interface in WMLES is usually not known a priori. A practical way to determine a proper FRPM mesh resolution is to set it to the same spacing used in the spanwise direction of the LES-TAU mesh, which corresponds to $1/20\delta_0$. In the tested simulations this led to roughly 20 to 25 cells over the boundary layer height with the mesh extending a bit outside the boundary layer edge. The reason is to have particles for the internal FRPM filtering operation, although the TKE is zero outside the boundary layer so that no turbulent velocity fluctuations are expected. It is merely

a measure taken to prevent possible artifacts without adding any significant strain in terms of computational cost.

4.1.6   Langevin time decorrelation

This option activates a temporal decorrelation. Without this option FRPM generates frozen turbulence which means the turbulent structures do not change in the streamwise direction. It is calculated with $1/(C_\mu \omega)$, where ω is the specific dissipation rate from the SST solution and $C_{mu} = 0.09$.

4.2   FRPM standalone results

In the following, results of using different FRPM parameters are presented. The goal is to find settings that produce vorticity fluctuations, hence velocity fluctuations, well suited for the transition from pure RANS modeling to WMLES. In theory, this should be the case for the synthetic turbulence with the closest resemblance to the specific real world turbulence.

FRPM is based on turbulence statistics such as the TKE and empirical quantities such as a length and time scale. These quantities are taken from a solution of the Menter-SST model implementation in the DLR TAU-solver. Using these turbulence statistics a first consistency check should be performed whether FRPM reproduces these statistics as intended. The ideal "FRPM-turbulence" would at least closely match the SST statistics, such as the TKE. This obviously does not imply a perfect match of the time-averaged SST statistics with the same real-world quantities, as there is no such perfect turbulence model. Different models will generally give different solutions. That topic is slightly touched upon in section 5.4.1 as FRPM is based on Menter SST statistics, while the SA-model is the underlying turbulence model in the investigated HRLES simulations.

As FRPM uses turbulence statistics from a prerun Menter SST k-ω simulation, and TKE is the variance it aims to reconstruct, matching the SST turbulence kinetic energy serves as the basis for assessing whether FRPM generates synthetic turbulence as intended.

In the following, FRPM results for matching the SST TKE for the different investigated test cases are shown. They are based on the practical approach described in section 4.1.5.

4.2.1   Flat plate patch

Figs. 4.1 and 4.2 show the turbulence kinetic energy for the flat plate FRPM patch for $lfac = 6$ and $lfac = 3$, respectively. It's equidistant grid spacing in the stream-, spanwise and wallnormal directions is $1/20\delta_0$. It is observed that different settings for lmin lead to different TKE reconstructions. Especially near the wall where the length scales quickly decreases, kinks in the TKE appear too small for settings for lmin and the TKE does not go to zero as it theoretically should.

The settings applied in later simulations for $lfac = 6$ correspond to $lmin = 0.0012$ as this showed the closest resemblance of the SST TKE, although the TKE is not fully resolved down to the wall. $lfac = 3$ in the FRPM-TAU coupling corresponds to the FRPM turbulence reconstruction for $lmin = 0.0009$.

An observation for the flat plate FRPM patch is that $lfac = 6$ results in a peak closer to the wall with greater magnitude than when smaller integral length scales are used with $lfac = 3$.

4.2.2   BFS patch

$lfac = 3$ was used because no TKE reconstructions were found to show close resemblance with the target TKE for $lfac = 6$, as the latter generally resulted in exaggerated peaks with kinks
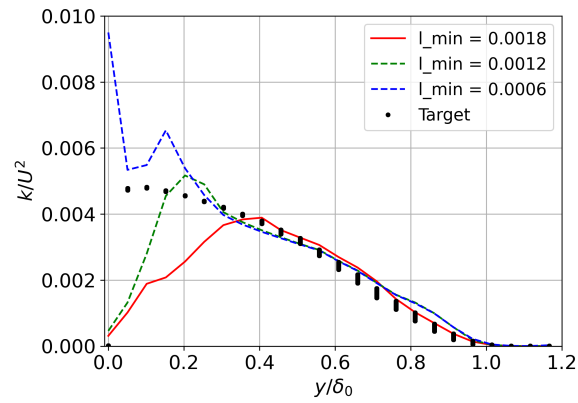
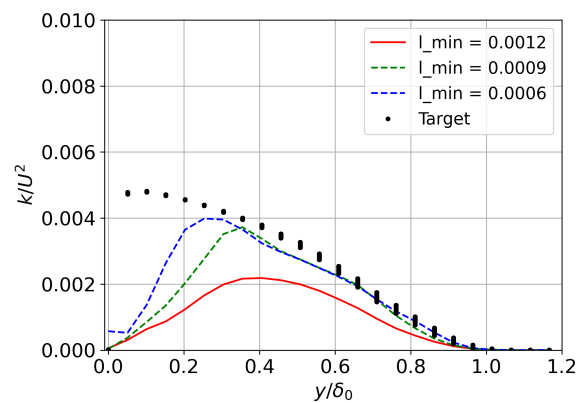**Figure 4.1:** The TKE generated with FRPM for $lfac = 6$.

Figure 4.2: The TKE generated with FRPM for $lfac = 3$.

near the wall. A value of $lmin = 0.0024$ was found to show the best results in combination with $lfac = 3$.

4.2.3 F15 patch

In the case of the DLR-F15, the interpolation from the TAU F15 SST solution onto the FRPM patch was found to be tricky as wavy structures appeared. This is depicted in fig. 4.3 and resulted in the solution shown in fig.4.4. The latter was observed to have unrealistically high peaks in the TKE in parts directly at the surface. Due to this observation and the time constraints of the work, no emphasis was placed on finding a solution and a refinement of the TAU mesh would have been too time consuming, i.e., it would have required a new SST solution on the newly created mesh which would have then been interpolated onto the FRPM patch.
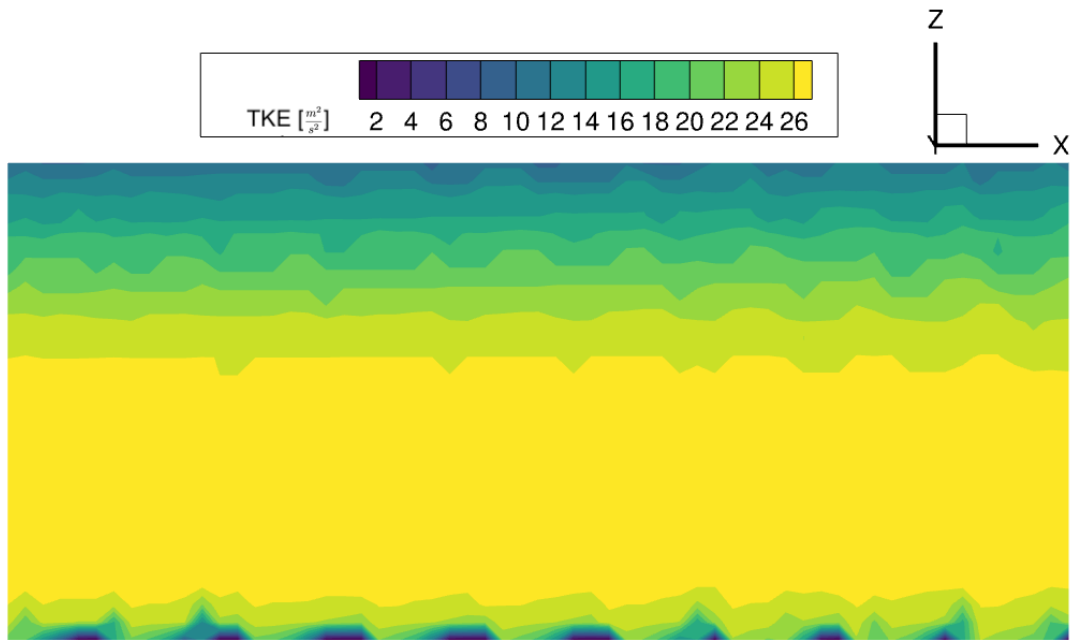
Figure 4.3: The TKE interpolated onto the FRPM patch for the F15 multi-element airfoil.
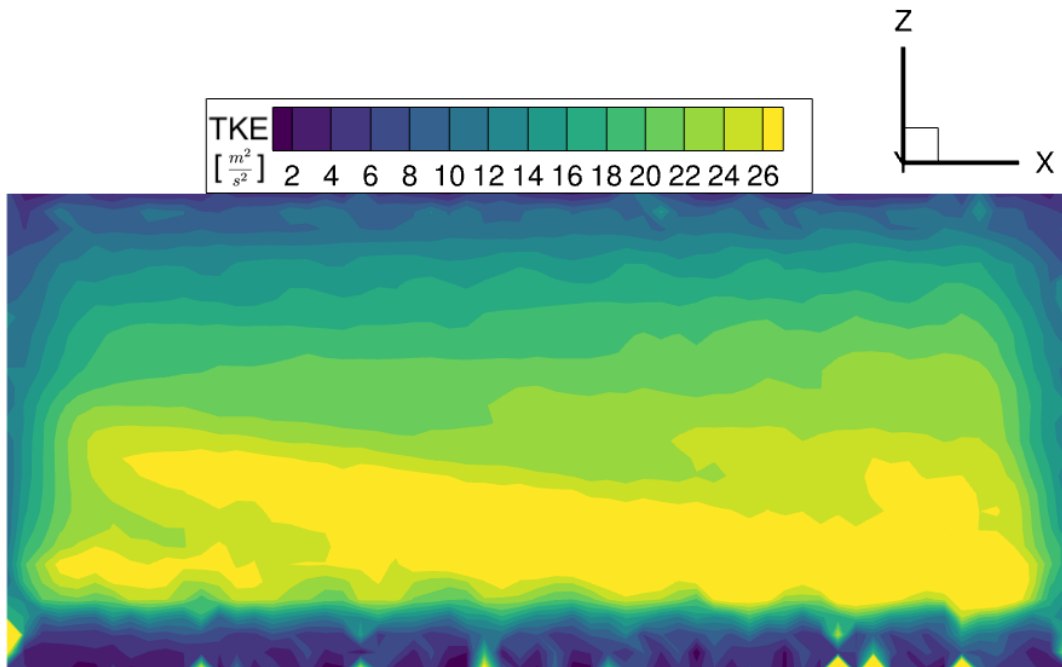
Figure 4.4: The TKE reconstruction for the F15 multi-element airfoil.

Chapter 5

FRPM-TAU: Coupling

In this chapter results of the actual coupling of FRPM with the DLR TAU solver are presented. First, the initial settings based on the FRPM manual are described and then continues with modifications to the setup. The goal is to find best-practices for its intended use to create turbulent content for a WMLES simulation, although the sensitivity study is mainly performed for the flat plate. A TAU mesh sensitivity study is performed in section 5.2. FRPM is explored both in terms of its aerodynamic and aeroacoustic prediction capabilities, with focus on the former.

5.1   FRPM-TAU: Sensitivity study

Unless stated otherwise, the following plots show solutions that were time-averaged for 15000 unsteady physical time steps, starting from an unsteady turbulent boundary layer that did not experience any significant change in its mean quantities. In addition, the solutions were spatially averaged in the spanwise direction. $x/\delta_0 = 0$ refers to the location of the RANS-WMLES interface.

The parameters varied include $lfac = 3$ (section 5.1.2) and $lfac = 6$ (section 5.1.4), which affect the size of the synthetically created turbulent structures. In both sections the effect of σ in the eddy-relaxation term is evaluated, which is one of the prime factors for the success of the investigated FRPM-TAU method. Improvement is then sought through injection of more realistic turbulence by adding a temporal decay. This is enabled by the Langevin option in FRPM (section 5.1.3). Next, the length of the FRPM patch is altered (section 5.1.5), which would, among other reasons, facilitate an integration of FRPM into more general flow cases, e.g., more spatially constrained geometries.

With respect to the FRPM part of the setup, i.e., parameters such as the length scale and underlying mesh, the synthetic turbulence corresponds to the results presented in chapter 4, where results of the synthetic turbulence without TAU coupling are discussed. $Lfac = 3$ and $Lfac = 6$ refer to the corresponding FRPM results, as these are FRPM specific parameters and cannot be set in TAU.

The coupling parameter σ in the eddy-relaxation term is expressed in multiples of the maximal eddy-viscosity on the FRPM patch. The eddy-viscosity is taken from the Menter SST $k - \omega$ model. For the flat plate patch it varies from nearly zero at the wall to $0.00159687 \frac{m^2}{s}$ at its maximum. The eddy-viscosity increases with increasing distance from the wall, reaching its maximum at approximately one third of the boundary thickness and then starting to decrease towards the edge of the boundary layer. σ, on the other hand, is treated as a control parameter and is kept constant over the entire injection region.
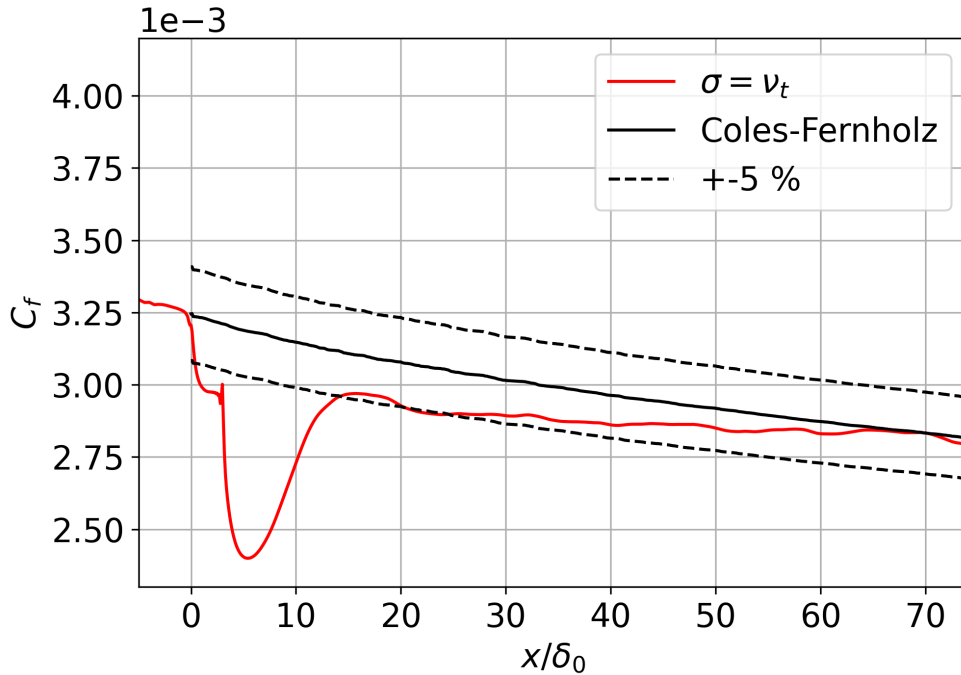
Figure 5.1: Results for the skin friction for lfac=6.

5.1.1 Initial setup

In this section, results of an initial FRPM-TAU setup are presented. The synthetic turbulence is based on handbook settings found in the FRPM manual. Specifically, $lfac = 6$ for isotropic turbulence is used. In section 2 it is stated that for the eddy-relaxation term a value for σ roughly the size of the eddy viscosity is appropriate. Thus, the maximal value $\nu_{t,max}$ on the FRPM patch is chosen for the initial setup. The synthetic turbulence is injected over a length of $3\delta_0$.

As discussed in section 1, the skin friction coefficient C_f is an important measure to evaluate whether the injected turbulence is able to fulfill the quality criteria in a HRLES setup, e.g., a short adaption region.. It is a particularly important measure for aerodynamic predictions and thoroughly discussed for the initial FRPM-TAU setup in the following.

The results for C_f are shown in fig. 5.15. In an ideal simulation one would transition from RANS modeling upstream to resolved turbulence downstream of the RANS-WMLES interface without seeing any deviation in the skin friction. It would perfectly match C_f of the Coles-Fernholz reference, also shown in fig. 5.15. In theory this should be realized with an ideal synthetic turbulence generator, accompanied with ideal injection. Since there is no such perfect method, deviations from the ideal behavior are expected. Here, synthetic turbulence is injected over a length of $3\delta_0$, starting from the $\frac{x}{\delta_0} = 0$ location where the RANS-WMLES interface is located. Transitioning from pure RANS modeling upstream of this position to the WMLES region, an initial drop with steep slope in C_f is observed. This rapid decrease takes place over a very short streamwise distance. Then C_f stabilizes on a lower level with slightly downward tilted slope which is parallel to the Coles-Fernholz reference. As the flow leaves the injection region, an additional more significant drop in C_f of $\approx 20\%$ in relation to the reference occurs. It is a broader and more significant dip compared to the initial dip of $\approx 7\%$ and extends roughly $11\delta_0$ downstream.

An explanation for the initial dip in C_f is that C_f is highly dependent on the total shear stress, and the modeled part of the total shear stress is quickly reduced as the turbulent viscosity

(a) Modeled $< u'v' > /U^2$

(b) Resolved $< u'v' > /U^2$

(c) Total $< u'v' > /U^2$
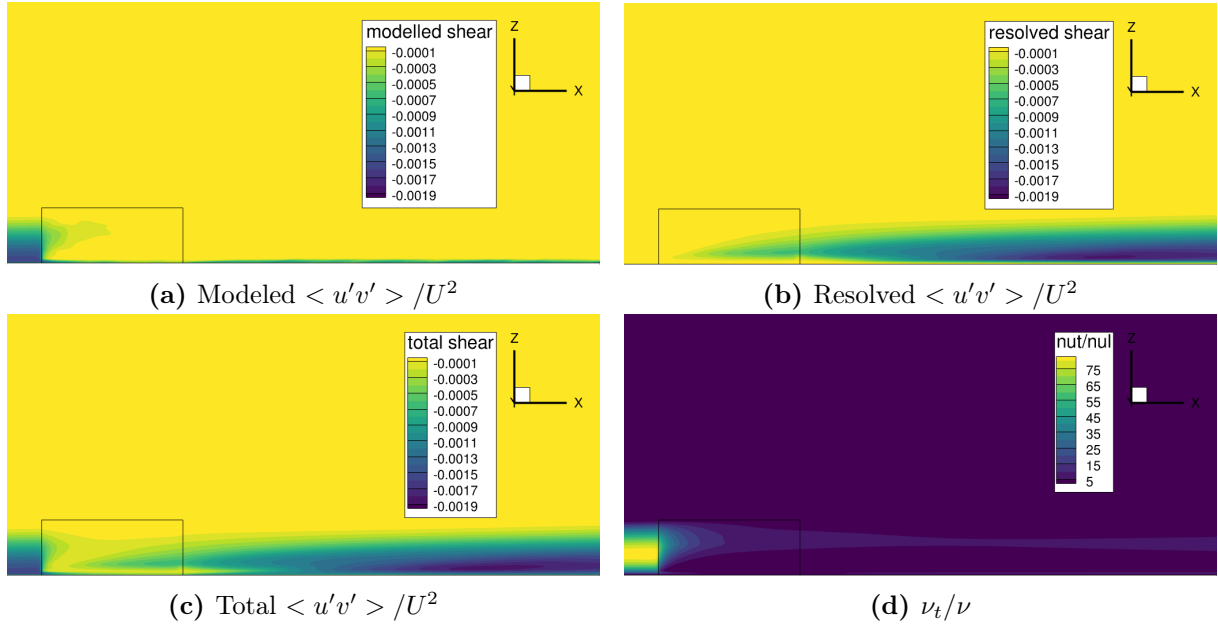

(d) ν_t/ν

Figure 5.2: Turbulent stresses averaged in the spanwise direction. Results were obtained for $lfac = 6$ and $\sigma = \nu_t$. The FRPM patch is visualized as the rectangular box.

decreases. The injected turbulent fluctuations then start to trigger enough resolved stresses to gradually stop the drop in C_f. Figs. 5.2a and 5.2d show this reduction in modeled shear stress and eddy-viscosity. At the same time the resolved shear stress needs time to develop and is not yet able to compensate for the strongly reduced modeled shear. It is notable how the near wall modeled stress is strongly reduced over the injection region and as the end of the injection region is reached one can observe the second more severe drop in C_f. The latter can be explained by the removal of the synthetic vorticity fluctuations which need to be compensated for by the WMLES equations. Therefore, downstream of the FRPM patch the near-wall modeled stresses again start to increase in magnitude and C_f recovers to within 5% below the reference level. The almost horizontal slope for $\sigma = 1\nu_{t,max}$ then slowly returns C_f back to the reference curve. However, from $11\delta_0$ downstream of the injection region C_f is no more than 5% from the reference level.

Another way to look at this quantitatively is by extracting slices at different stations x/δ_0 downstream of the RANS/WMLES interface. The corresponding Reynolds stresses and viscosity levels are depicted in fig. 5.3. They correspond to the same solution shown in fig. 5.2 at different downstream locations x/δ_0 of the injection region. To explain the dip as the injection region is exited, it is useful to look at stations associated with the dip in C_f and compare them with results at $x/\delta_0 = 13$ where C_f has recovered to within 5% of the reference. One could expect the total shear to have a similar trend as C_f and there to be less total shear in the wall region. However, there is no reduction in the total shear stress in fig. 5.3d, rather there is a continuous growth in this component, even throughout the C_f dip region. Therefore, it alone does not explain the drop. Below, another observation is made in terms of the near wall velocity gradient $\frac{du}{dy}$ which gives better insight to the cause. However, it is also worth looking at the normal stresses, as they give additional insight into what happens as the turbulence leaves the injection region.

The development of the normal stresses $< u'u' >$, $< v'v' >$ and $< w'w' >$ downstream of the injection is shown in figs. 5.3a, 5.3e and 5.3f, respectively. The resolved $< u'u' >$ and $< w'w' >$ stresses show a continuous increase downstream of the injection region. However, this is not observed for the wall normal stress component $< v'v' >$. Here, the trend is an initial decrease in the $< v'v' >$-maximum from $x/\delta_0 = 3$ to at least $x/\delta_0 = 6$, coinciding with the decrease in C_f. One can see that at $x/\delta_0 = 6$, which corresponds to the location of the minimum C_f value, the slope in the $< v'v' >$ component from $y/\delta_0 = 1e - 3$ to the location of the $< v'v' >$ maximum

is shallower than at any of the other shown downstream locations. Other than that, a shift of the near wall $< v'v' >$ towards the wall is seen, so that near the wall $< v'v' >$ actually increases downstream. The reduction in the $< v'v' >$ maximum which is then followed by an increase shows that the turbulence is still developing because a clear trend would be expected for the flat plate boundary layer.

In fig. 5.3, the overall observation is made that all of the stresses stay below the reference stresses taken from the upstream SA-RANS at $x/\delta_0 = 0$, except for the peak in the $< u'u' >$-component. The SA-RANS reference stresses would change in the downstream direction but in any case it is not expected to give a perfect match with the real-world stresses. Rather, it serves as an approximate reference for the expected magnitudes.

Looking at ν_t/ν in fig. 5.3g, the already noted increase in the turbulent viscosity in the downstream direction is seen. This indicates an increase in RANS modeling near the wall. The reduction of this increase indicates that the boundary layer is reaching a stable level of RANS modeling in terms of the WMLES boundary layer. Up to this point the boundary layer is still undergoing strong development.

Next, the instantaneous velocity fluctuations are presented in fig. 5.4 to show the aforementioned development of the flow field. It is clearly seen how the turbulent structures injected through the eddy-relaxation term have a rounded, almost isotropic shape. This is due to the isotropic nature of the turbulent structures generated in FRPM (other anisotropy-modeling versions of FRPM exist but were not investigated in this study). As the turbulence exits the injection region, its vortices gradually transform into more realistically stretched and elongated vortices. Maturely developed turbulence is seen in the right half of the figure. It corresponds to the region of at least $12\delta_0$ behind the FRPM outflow where C_f has mostly recovered. An ideal synthetic turbulence generator would inject turbulence perfectly resembling the fully developed and mature turbulence (of course with appropriate and perfect scaling for its upstream location). Since this is not the case for any current synthetic turbulence, it requires some adaption distance over which the deviation in C_f occurs and where the turbulence changes its shape as shown in fig. 5.4.

As the flow moves through the turbulence injection region it can be associated with a mean velocity profile. The spanwise averaged logarithmic velocity profile for the different slices are plotted in 5.5a. An almost perfect match is obtained at the outflow of the synthetic turbulence generator at $3\delta_0$. As the injection area is exited, the turbulent structures go through the aforementioned transformation which affects the velocity profile at the indicated downstream locations. This alters the near wall velocity gradient $\frac{du}{dy}$ which directly goes into the equation for C_f. $\frac{du}{dy}$ is shown in fig. 5.5b. $\frac{du}{dy}$ is largest at $x/\delta_0 = 3$ and $x/\delta_0 = 15$ and smallest at the stations where the dip in C_f occurs. Thus, a significant decrease in $\frac{du}{dy}$ is observed when leaving the injection region. The total shear stress, on the other hand, keeps increasing. Therefore, a delay between the velocity gradient and the acting shear stresses is evident.

A downside of injecting synthetic turbulence is the common problem of producing nonphysical spurious noise, as discussed in chapter 1. The result of this measure is presented in fig. 5.6, where P denotes the reference pressure of $99120Pa$. Some wiggles in the pressure fluctuations can be observed but are negligible in magnitude in comparison with other synthetic turbulence generators, such as the STG. This is shown in the next chapter.

To conclude this section, a significant under-prediction of C_f was observed in this initial FRPM-TAU setup. It is the result of a significant under-prediction of the total shear stress and its slow increase to higher levels. Further, a delay of the mean velocity gradient $\frac{du}{dy}$ following the shear stress increase was seen. This was shown to lead to a significant dip in C_f. However, full recovery to its reference level was achieved.
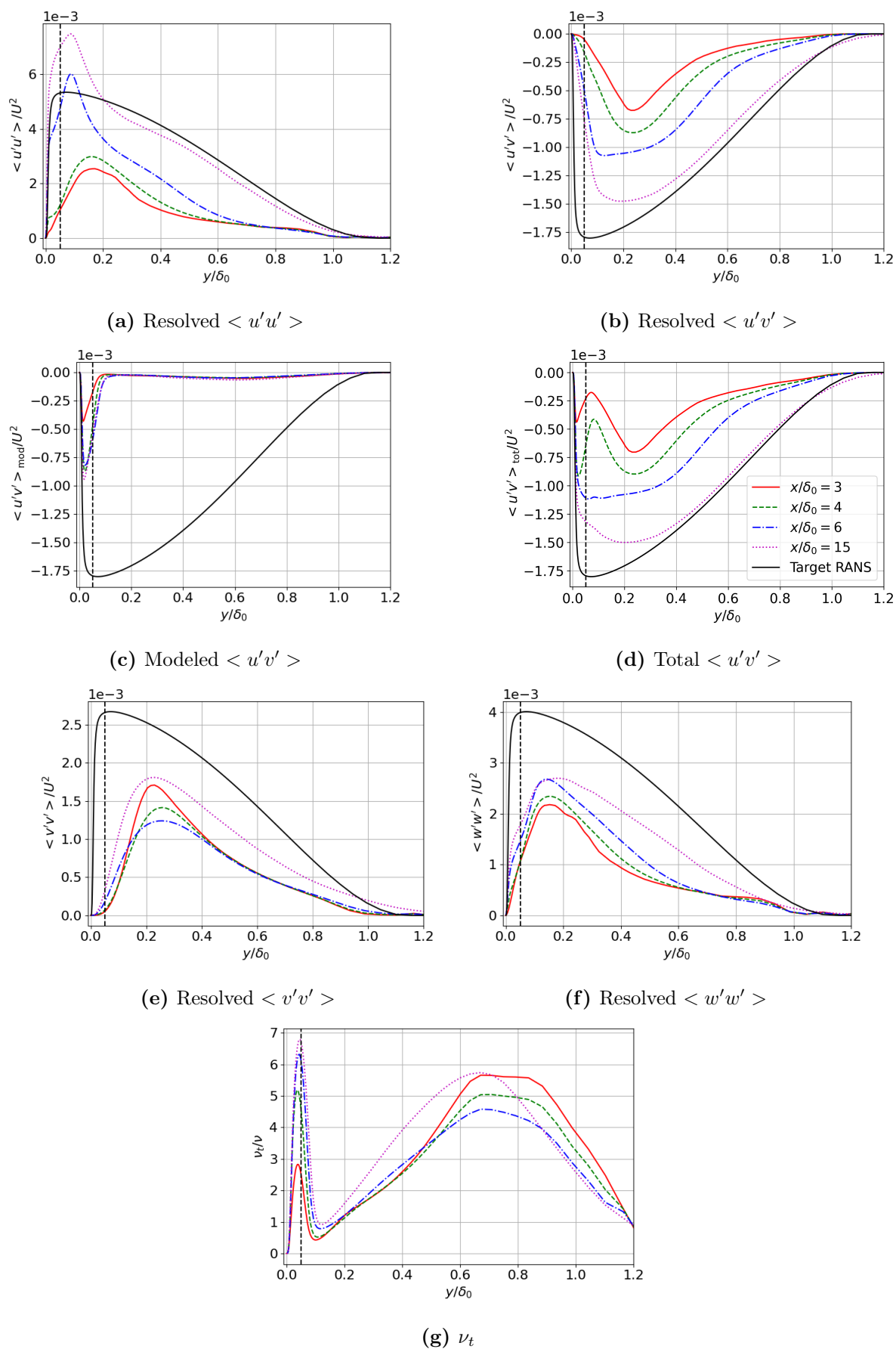
(a) Resolved $< u'u' >$

(b) Resolved $< u'v' >$

(c) Modeled $< u'v' >$

(d) Total $< u'v' >$

(e) Resolved $< v'v' >$

(f) Resolved $< w'w' >$

(g) ν_t

Figure 5.3: Turbulent stresses at different downstream locations for the initial setup.
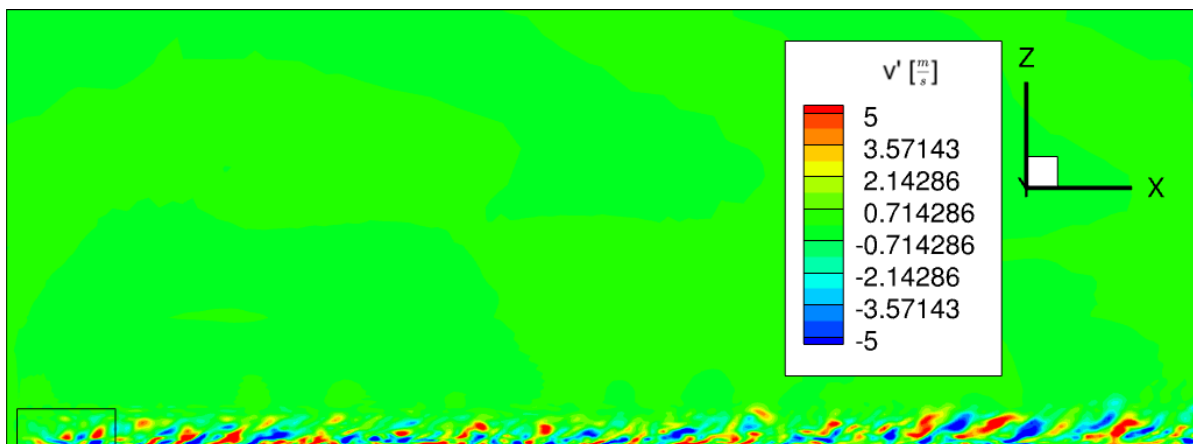
Figure 5.4: Instantaneous spanwise velocity fluctuations for $\sigma = \nu_t$ and $lfac = 6$.
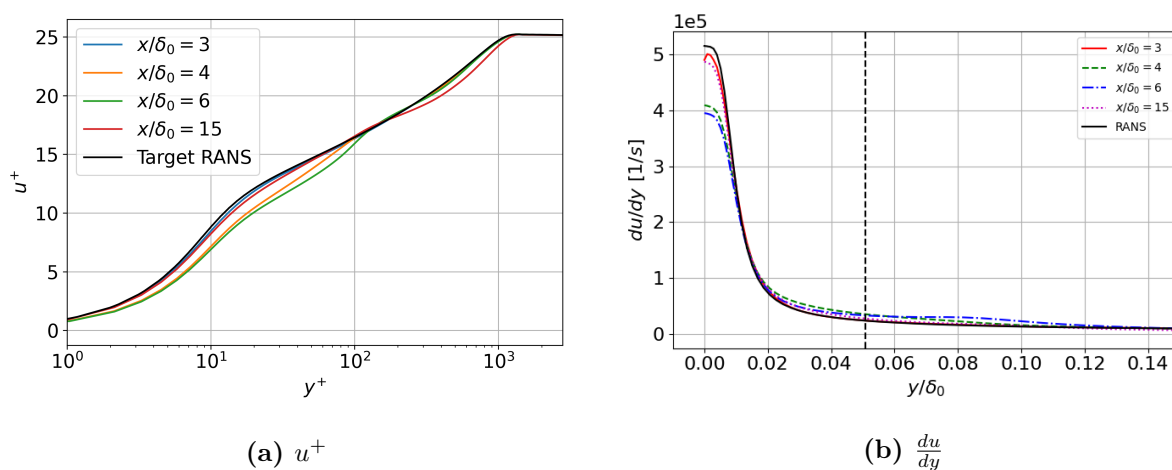

(a) u^+

(b) $\frac{du}{dy}$

Figure 5.5: Spanwise averaged logarithmic velocity profiles and near-wall velocity gradients for the initial setup.
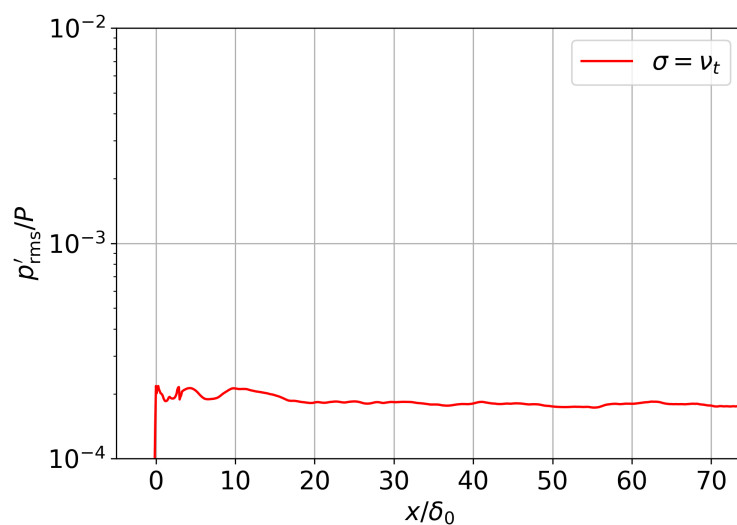
Figure 5.6: Pressure fluctuations for the initial setup with $lfac = 6$.

5.1.2 Lfac=3 and varying σ

In this subsection the initial setup is altered, aiming at a reduction in the C_f-dip. This issue is thoroughly discussed in section 5.1.1. In the following study, $lfac = 6$ is lowered to $lfac = 3$, while further investigating the effect of different values for the coupling parameter σ.

The main drawback observed in the initial setup is the under-prediction of the skin friction, which showed up as a large dip just downstream of the injection region, while good performance was achieved in terms of not producing unwanted spurious noise. Honing in on the C_f-dip, it was mainly attributed to an under-prediction in total shear and a reshaping of the injected turbulence towards a more realistic one, leading to the adaption region of over 10 δ_0. In this subsection the issue is tackled by varying the coupling parameter σ in the eddy-relaxation term. This parameter determines how closely the resolved fluctuations are forced to follow the synthetic ones. Increasing σ yields a closer coupling between the resolved and synthetic fluctuations, also forcing the resolved TKE closer to the FRPM target. Therefore, the idea with higher values of σ is to trigger higher magnitude resolved velocity fluctuations and generally trigger higher stresses. A closer resemblance with the synthetic turbulence within the injection region is also a logical goal since ideally it is the closest one can get to the real turbulence and this is the underlying principle of the method. However, no synthetic turbulence, including FRPM, is perfect and has its limitations in terms of reproducing realistic turbulence. This fact can influence the choice of σ. Real world turbulence is characterized by anisotropy, for example near a wall. In terms of vortical structures, a deformation and stretching would be expected. This anisotropy is not modelled in the synthetic turbulence created in this work. Therefore, high values of σ would force the solution towards one with less anisotropical behavior. Lower values on the other hand would free the resolved turbulence from this constraint and give more leverage to the CFD-solver to fill in this missing anisotropy. This is the reasoning for testing various values σ, instead of merely choosing the largest value possible.

The idea behind reducing $lfac$ in FRPM is as follows. It was reduced from $lfac = 6$ to $lfac = 3$, as this results in smaller eddies and a smoother variation in the FRPM filter width, which may be beneficial in the near-wall region where the length scale is quickly decreasing. Further, it must be kept in mind that $lfac = 6$ is derived for isotropic turbulence [3] but close to the wall the turbulence is far from isotropic in terms of its characteristic stresses and structures due to the constraint of the wall and viscosity. Results for $lfac = 3$ are presented below.

In comparison to the initial setup in fig. 5.15 with $lfac = 6$ and $\sigma = \nu_t$, the same drop in C_f is observed over the extent of the injection area. However, as the turbulent flow leaves the injection region, an even stronger dip in C_f occurs. Another issue is the nonexistent recovery. There is a recovery, but it is more than 10% below the Coles-Fernholz reference, followed by a downward tilted slope that is comparable to the reference.

Increasing σ to twice or three times its initial value does increase C_f over the injection region, lining up with the expectation. It is not sufficient, however, to reach the reference level and stays 5% below the reference even for $\sigma = 3\nu_t$. Higher values of σ led to non-converging solutions with $CFL = 10$, which was the selected CFL-number in order to keep the simulation wallclock time within a few days. As can be observed in fig. 5.7, no major improvement is expected from higher σ's anyway. Comparing the solutions for $\sigma = 2\nu_t$ and $3\nu_t$, the differences are minor, while a more significant improvement is gained over $\sigma = \nu_t$. The trend is that higher values of σ asymptotically converge to the same solution. Theoretically that solution is reached as soon as the resolved and synthetic fluctuations match. Further note that in section 5.1.4 it is observed that for $\sigma = 3\nu_t$ and $lfac = 6$ the unsteady turbulent boundary layer is still developing many boundary layer thicknesses downstream and this results in a more downward tilted slope. In that case averaging over the 15000 unsteady physical time steps would need to be postponed until the boundary layer does not change anymore. Obviously, this would result in an even longer overall
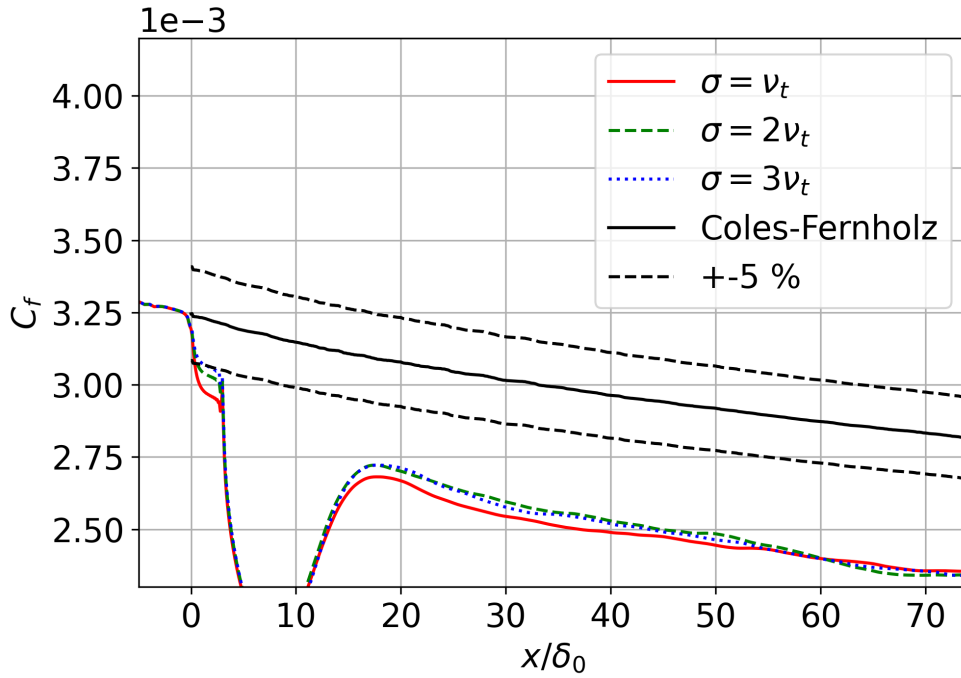
Figure 5.7: Results for the skin friction for lfac=3 and different values of σ.

simulation time.

Higher values of σ lead to higher normal stresses which is in line with the expectation and is shown in fig. 5.8. However, all components of the stresses, including the shear stress, show a deficiency when compared to the initial setup, even for $\sigma = 3\nu_t$. The shape and peak value of all normal stress components is at $y/delta_0 \approx 0.35$ and roughly reflects the shape and location of the peak value that was seen in conjunction with the corresponding FRPM standalone results for the TKE, (see section 4.2). The resolved shear does not follow the trend of increasing its magnitude with increasing σ. Rather, it shows an opposite behavior where the magnitude not only increases with lower values of σ but has its peak value moved closer to the wall. This can be explained with the aforementioned anisotropy argument because $lfac = 3$ only scales FRPMs isotropic turbulence and decreases the size of its turbulent structures. It does not add any turbulent shear stress on its own.

Compared to the initial setup, $\frac{\nu_t}{\nu_t}$ in fig.5.8g shows a higher peak value in the turbulent viscosity indicating a higher degree of modeling in the outer part of the boundary layer which is directly reflected in fig. 5.8c. Ideally, this region would show higher magnitudes in the resolved stresses, as the outer part of the boundary layer is the LES regime.

A good match with the logarithmic velocity profile is achieved for all σ's where the turbulence leaves the injection region, as seen in fig. 5.9a. This is also reflected in the near wall $\frac{du}{dy}$ which is similar to the initial setup, as expected due to the similar C_f magnitude over the injection region.

Very low levels of pressure fluctuations are observed in fig. 5.10. They are below the expected value that is of the magnitude seen towards the right side of the figure.

5.1.3   Langevin

In section 5.1.2 a continuous under prediction of C_f is seen without recovery to the Coles-Fernholz reference. By adding a temporal decorrelation, another layer in the modeling of realistic

(a) Resolved $< u'u' >$

(b) Resolved $< u'v' >$

(c) Modeled $< u'v' >$

(d) Total $< u'v' >$

(e) Resolved $< v'v' >$

(f) Resolved $< w'w' >$

(g) ν_t
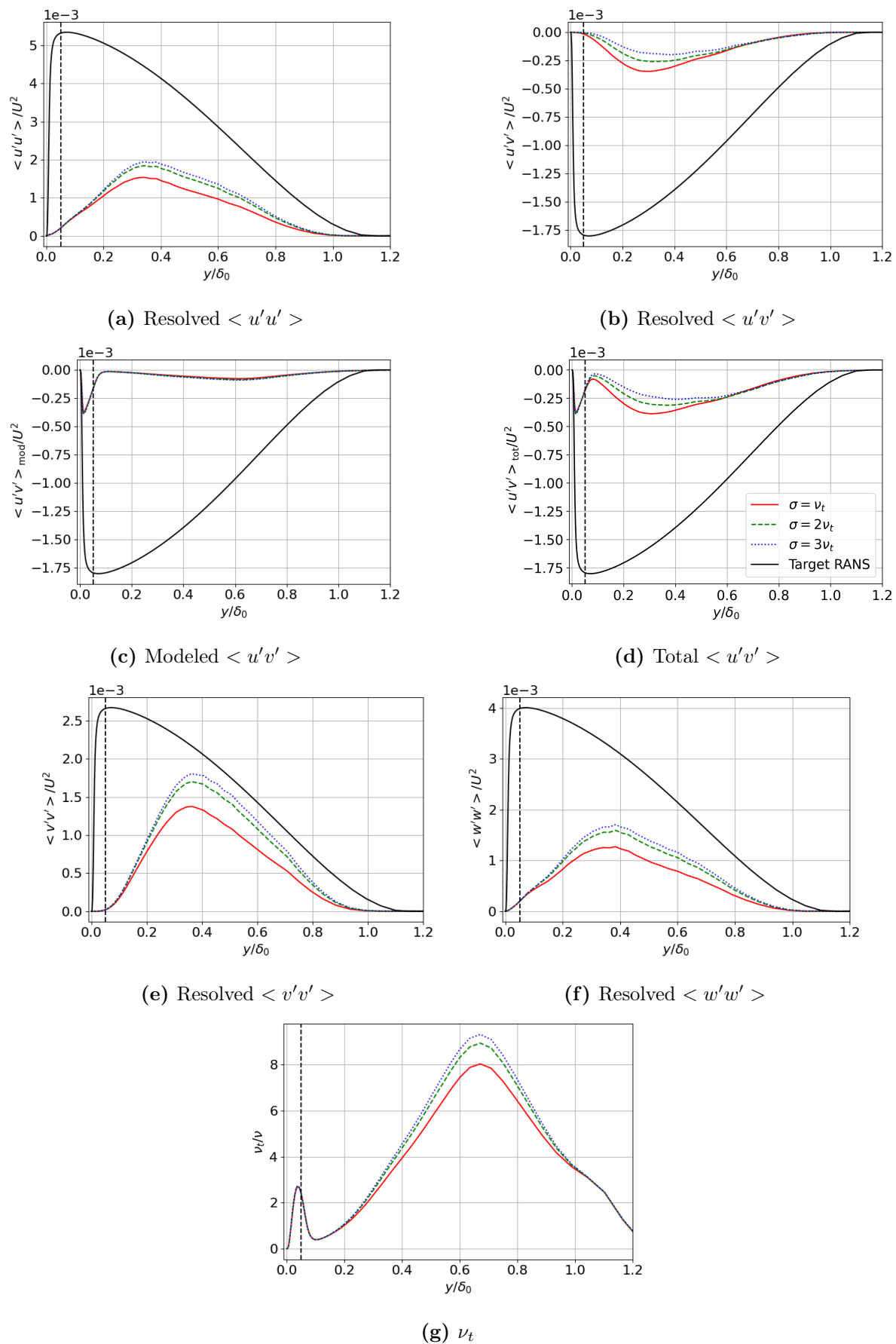
Figure 5.8: Turbulent stresses and $\frac{\nu_t}{\nu}$ for $lfac = 3$ and different values of σ at a distance of $3\delta_0$ behind the RANS-WMLES interface.

(a) u^+

(b) $\frac{du}{dy}$
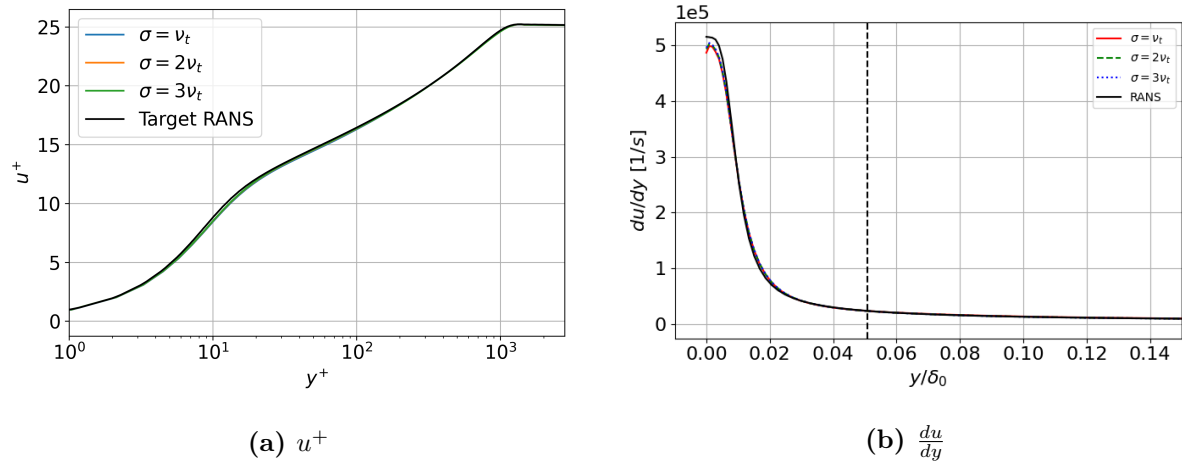
Figure 5.9: Spanwise averaged logarithmic velocity profiles and near-wall velocity gradients for $lfac = 3$ and differents values of σ.
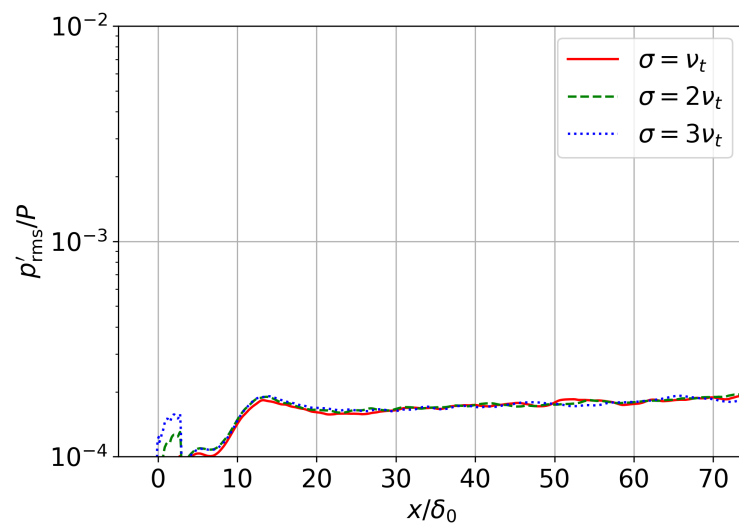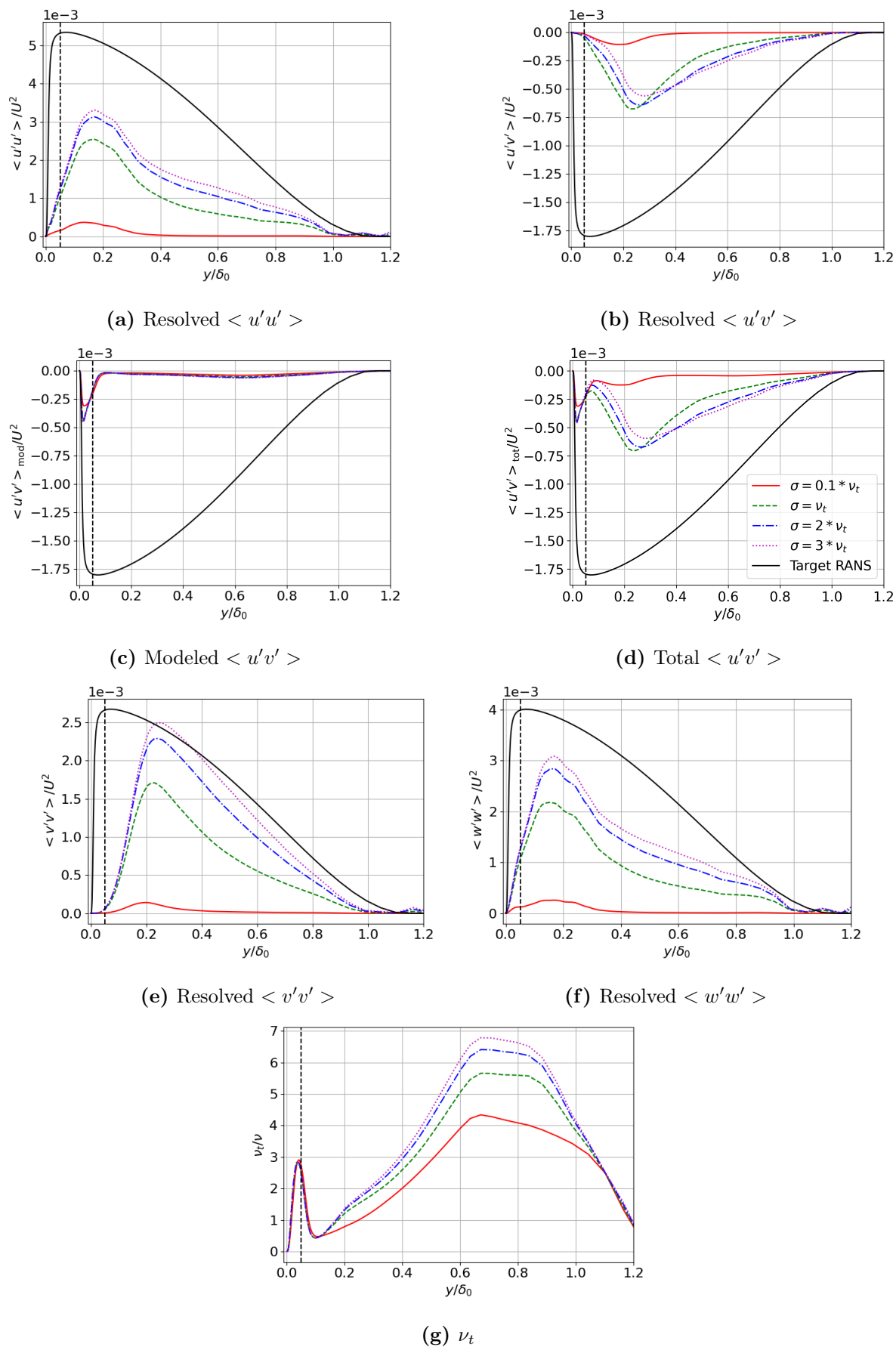

Figure 5.10: Pressure fluctuations
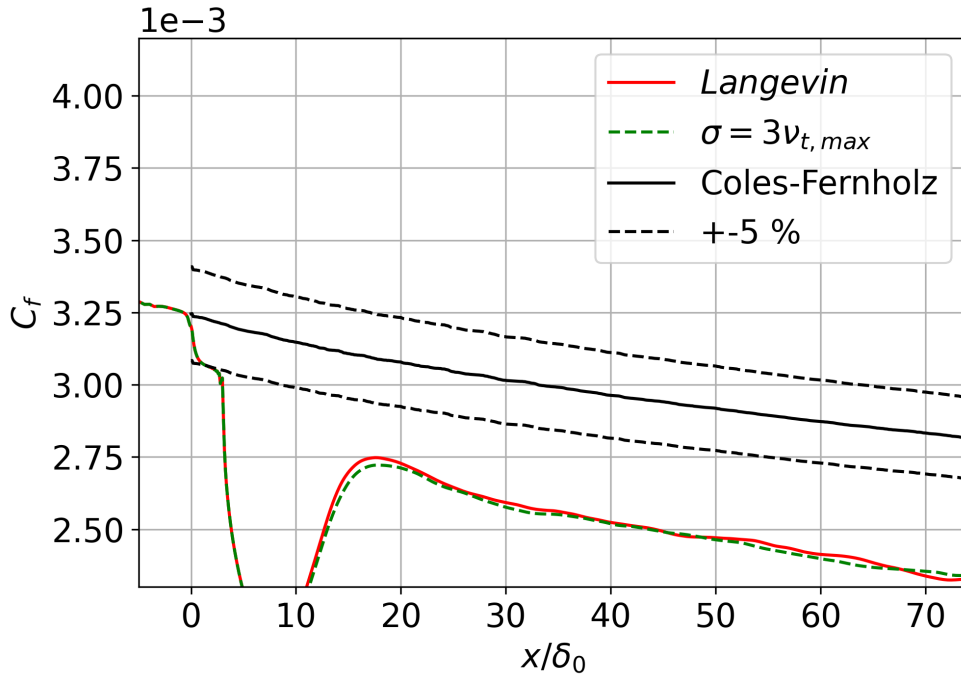
Figure 5.11: Results for the skin friction for lfac=3 and $\sigma = 3\nu_{t,max}$ with and without Langevin.

turbulence is added. In this case the turbulent structures are not "frozen" but vary in the downstream direction. The idea is that this can positively affect the development of the unsteady boundary layer downstream of the injection region and result in a full recovery of C_f and a shorter adaption length. Besides adding the Langevin time-decorrelation, the FRPM settings are unchanged from section 5.1.2. The results for C_f are shown in fig. 5.11. Modeling unsteady temporal decay does not yield any benefit over frozen turbulence in this simple flat plate test case.

This minor deviation in C_f is also seen in the stresses (fig. 5.12) and mean velocity profile (fig. 5.13).

5.1.4 Lfac=6 and varying σ

Since the smaller turbulent structures generated with FRPM, i.e., $lfac = 3$ showed poorer performance in their matching of the reference C_f when compared to the initial setup, $lfac = 6$ is investigated in this section as larger prescribed integral length scales may be beneficial in terms of achieving more intense turbulence downstream of the injection. This goes in hand with the results presented in fig. 5.15 and as seen in the initial setup which corresponds to the green, dashed line. Again, the main parameter varied in this section is the coupling parameter σ. As opposed to the smaller $lfac = 3$, different values for σ have more impact on the boundary layer's development for the larger integral length scales, although C_f is very close throughout the injection region for the corresponding σ's. Doubling the initial value of $\sigma = \nu_{t,max}$ leads to a full recovery of C_f approximately $12\delta_0$ downstream of the FRPM domain's exit. Further, results for a small $\sigma = 0.1\nu_{t,max}$ is shown. However, it seems not sufficient to stimulate big enough stresses. Even the near wall resolved shear stress in fig. 5.16b is small, in contrast to the trend discussed in section 5.1.2, which applies only to the larger σ's shown.

The trends are qualitatively the same as for $lfac = 3$ in section 5.1.2. However, the resolved stresses are of greater magnitude and this explains the increase in C_f. Furthermore, the closer to the wall peak of the TKE (fig. 4.1) for $lfac = 6$ is reflected in all components of the stresses.

(a) Resolved $< u'u' >$

(b) Resolved $< u'v' >$

(c) Modeled $< u'v' >$

(d) Total $< u'v' >$

(e) Resolved $< v'v' >$

(f) Resolved $< w'w' >$

(g) ν_t
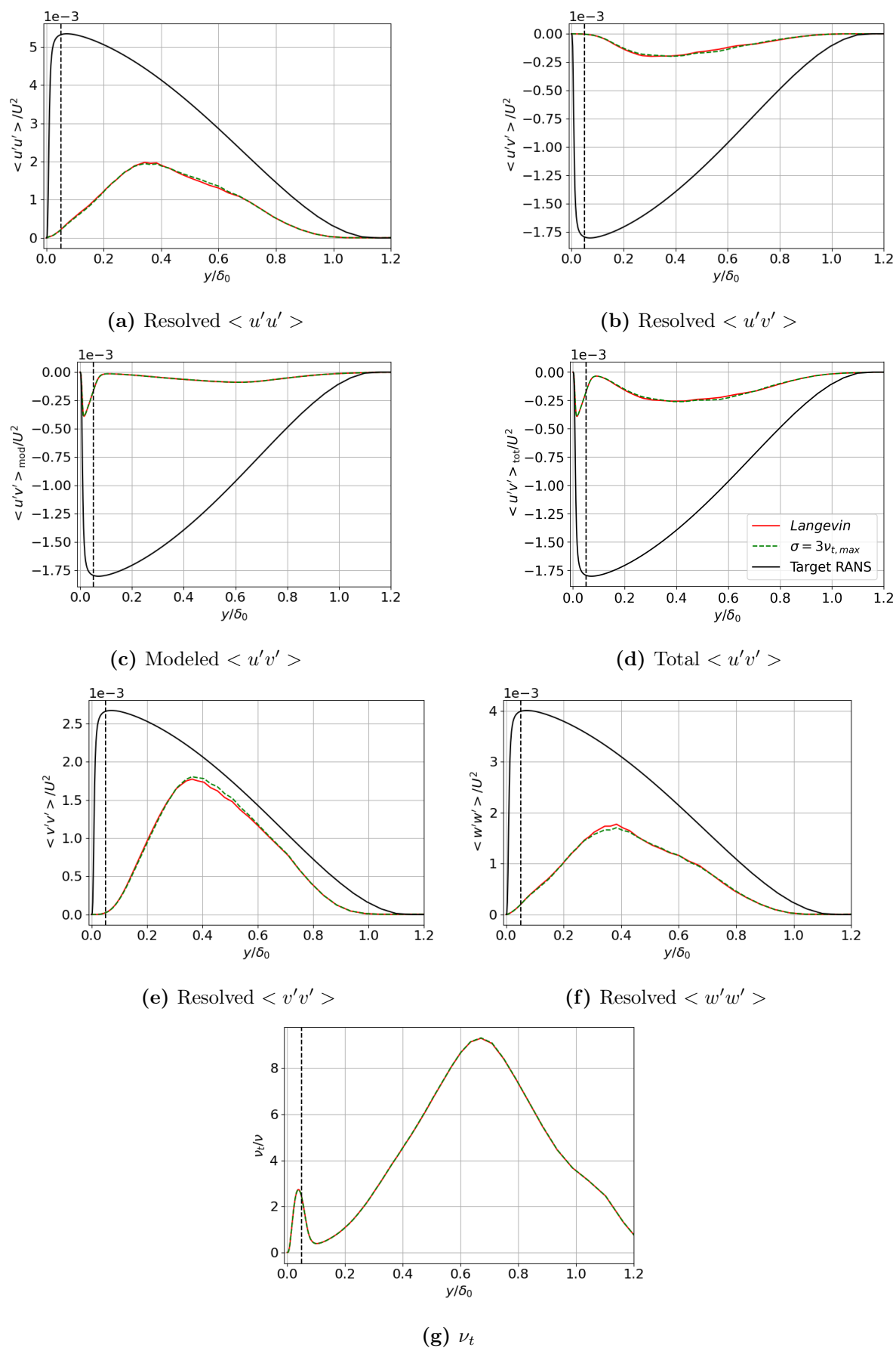
Figure 5.12: Turbulent stresses and $\frac{\nu_t}{\nu_t}$ for lfac=3, $\sigma = 3\nu_{t,max}$ with and without Langevin at a distance of $3\delta_0$ behind the RANS-WMLES interface.

(a) u^+

(b) $\frac{du}{dy}$
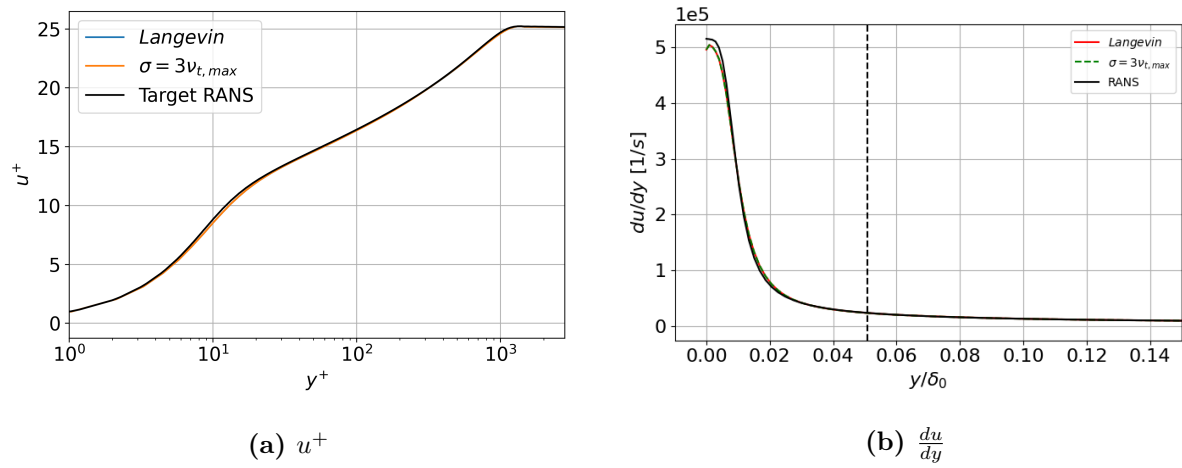
Figure 5.13: Spanwise averaged logarithmic velocity profiles and near-wall velocity gradients for lfac=3 and $\sigma = 3\nu_{t,max}$ with and without Langevin.
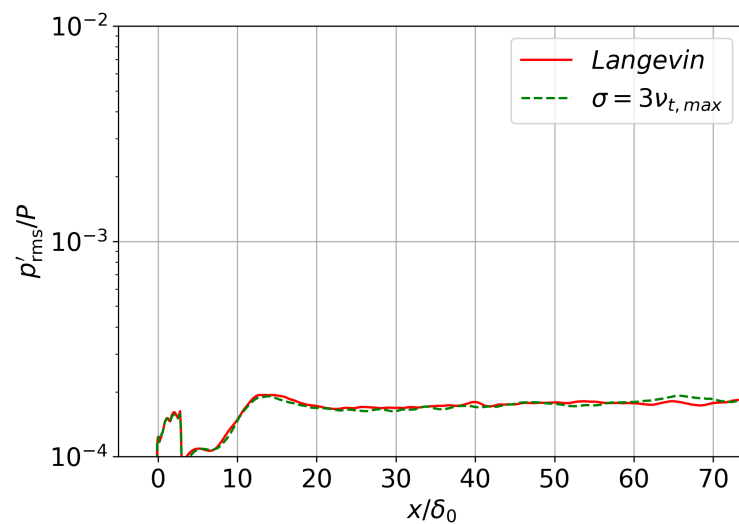
Figure 5.14: Pressure fluctuations
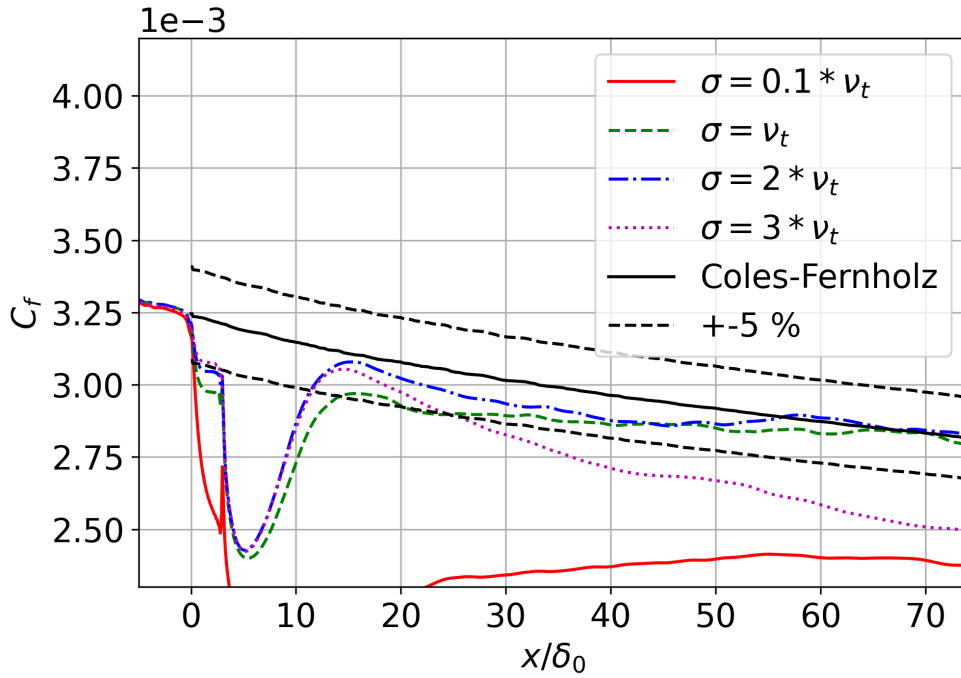
Figure 5.15: Results for the skin friction for lfac=6 and different values of σ.

As seen in fig. 5.9, good agreement with the RANS logarithmic velocity profile is observed for all values of σ as the flow leaves the FRPM domain, except for $\sigma = 0.1$. For the latter this leads to the comparably small $\frac{du}{dy}$.

In terms of unwanted noise production, a small increase of the overall pressure flucuation level seen in fig. 5.18. However, this is still comparably small when compared, for instance, to the STG. The increase in pressure fluctuation intensity seems to directly scale with the coupling strength of σ, with tighter coupling leading to a general increase, while the general shape over the injection region remains the same, with slight pressure fluctuation increases towards the FRPM in- and outflow.

5.1.5   FRPM patch length

Fig. 5.19 shows how C_f varies for different synthetic turbulence injection lengths in terms of multiples of δ_0. This is motivated by the fact that shorter lengths may be sufficient to effectively inject the same turbulent structures into the flow domain and therefore reduce the overall region of reduced skin friction, including the injection region (although the adaption region is defined as the length it takes for the turbulent flow to develop, measured from the synthetic turbulence's outflow). However, it is seen that shorter patches show less recovery of the skin friction and have lower minimums.

In terms of the pressure fluctuations the shortest patch length shows the smallest initial peak followed by a small region of lesser magnitudes. For patch lengths twice and three times as long, the elevated level goes in hand with the patch length as is expected.

5.2   FRPM-TAU: BFS

In this section results for the BFS are presented. The sensitivity of the solution to a varying TAU mesh in the injection region is investigated and presented in section 5.2.1. In lieu to changing the FRPM part of the coupling, as done in the sensitivity study for the flat plate, here, the sole

(a) Resolved $< u'u' >$

(b) Resolved $< u'v' >$

(c) Modeled $< u'v' >$

(d) Total $< u'v' >$

(e) Resolved $< v'v' >$

(f) Resolved $< w'w' >$

(g) ν_t

Figure 5.16: Turbulent stresses and $\frac{\nu_t}{\nu_t}$ for $lfac = 6$ and different values of σ at a distance of $3\delta_0$ behind the RANS-WMLES interface.

(a) u^+

(b) $\frac{du}{dy}$
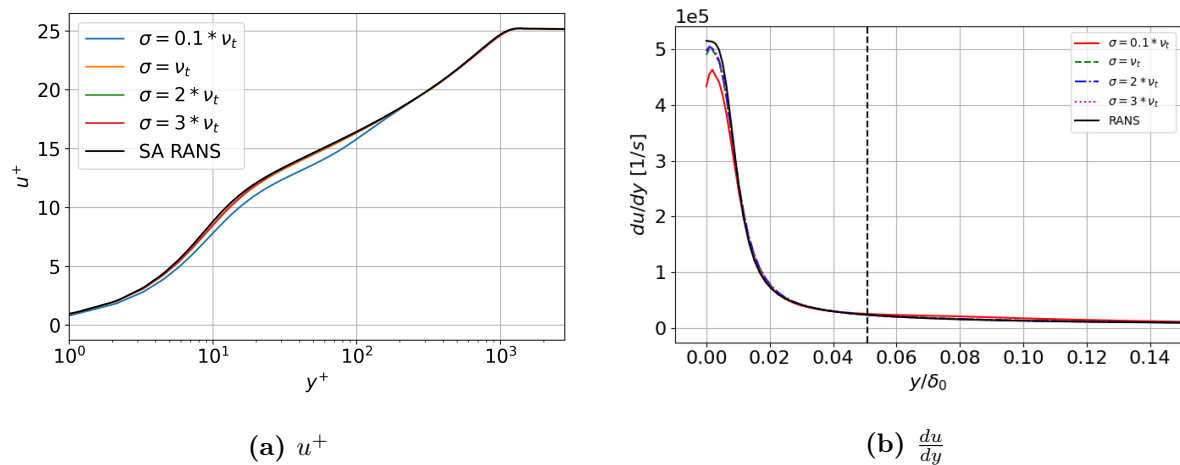
Figure 5.17: Spanwise averaged logarithmic velocity profiles and near-wall velocity gradients for $lfac = 6$ and differents values of σ.
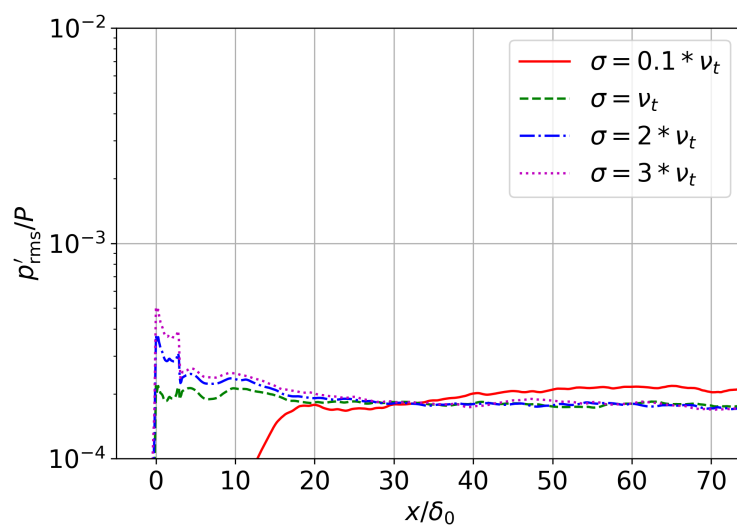
Figure 5.18: Pressure fluctuations
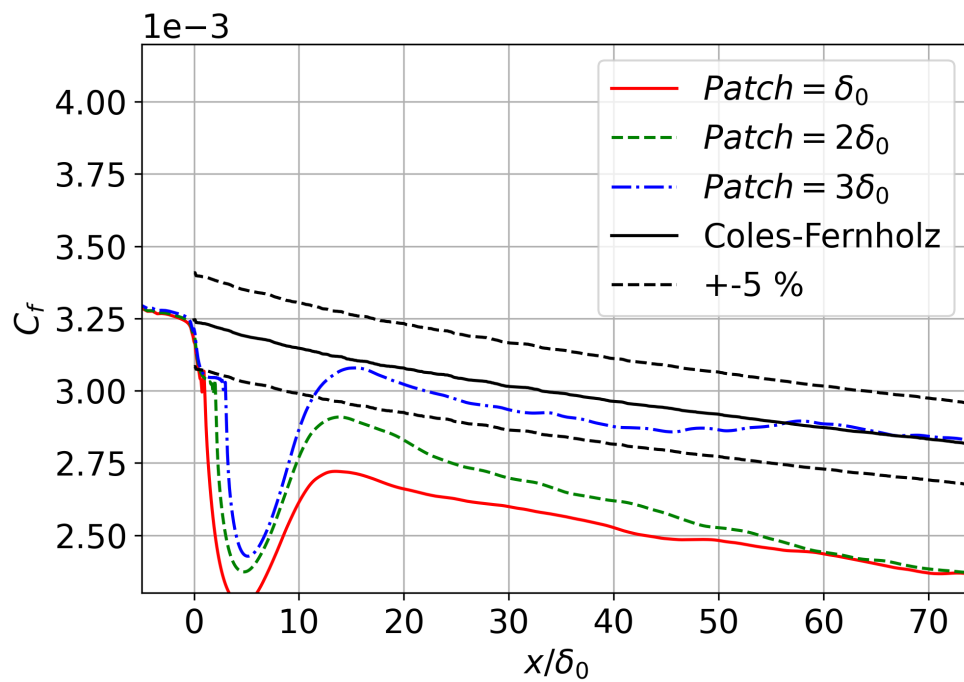
Figure 5.19: Results for the skin friction for different patch lengths.
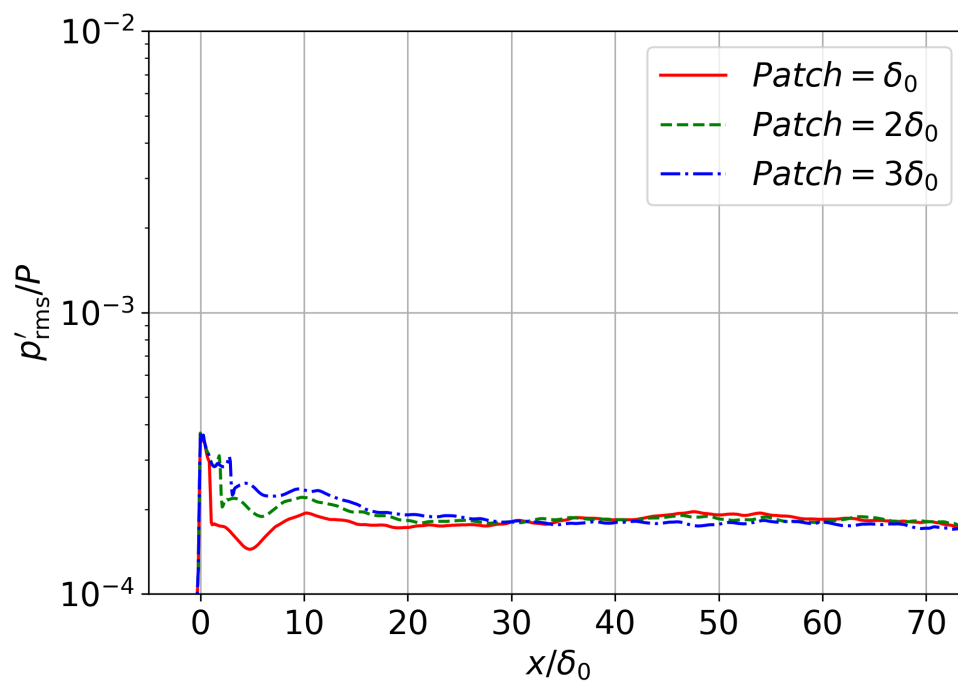
Figure 5.20: Pressure fluctuations for different patch lengths.
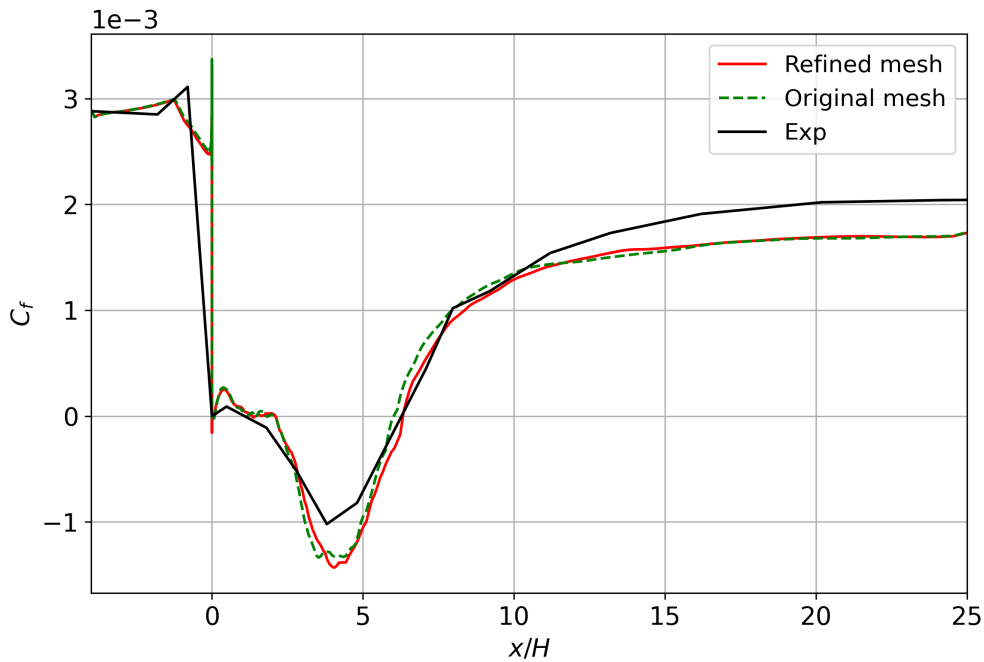
Figure 5.21: Results for the skin friction for the BFS test case are shown.

changes are performed to the TAU mesh. That means the FRPM settings and patch are the ones presented in section 4.2.2, i.e., $lfac = 3$. Averaging of the BFS solutions was performed over 30000 physical time steps as this led to smoother solutions just downstream of the step. However, it did not change the general magnitudes, such as of C_f. Experimental results for the skin friction and pressure fluctuations are provided as a reference.

5.2.1 TAU-mesh sensitivity

Fig. 5.21 shows how the skin friction varies for the two TAU meshes with the injection of turbulence at the inflow of the domain. The finer orthogonal grid with equidistant spacing in the streamwise direction shows no significant improvement over the DES grid. Both curves for C_f lie on top of each other upstream of the step. Minor insignificant deviations are seen downstream of the step. It is notable that the finer upstream grid perfectly matches the experimental data for the location of reattachment at $\approx 6x/H$ that follows the recirculation region behind the step. In both cases, C_f closely matches the reference in the injection region but drops off as the flow leaves the FRPM domain, followed by a peak directly at the step location. This initial dip may correspond to the bigger dip seen for the flat plate, also just downstream of the injection region. In this case a region with strong natural instabilities follows which could prevent the dip from significantly decreasing. The huge drop in C_f in the experimental data is just due to the lack of data directly at the step. As expected, negative C_f occurs in the recirculating area due to the flow reversal at the lower surface. Then it increases towards the reattachment region of the separated shear layer from the top, where $C_f = 0$, which is then followed by a continuous increase towards its final value towards the exit of the computational domain.

Fig. 5.22 shows the turbulent stresses at downstream locations of the step. As expected the development of the stresses when comparing both meshes is almost identical.

In terms of the pressure fluctuations in fig. 5.23, FRPM shows an under prediction over the entire injection region. Again, differences between the TAU-meshes are only seen in downstream of the step and are minor.

(a) Resolved $< u'u' >$

(b) Resolved $< u'v' >$

(c) Resolved $< v'v' >$

(d) Resolved $< w'w' >$
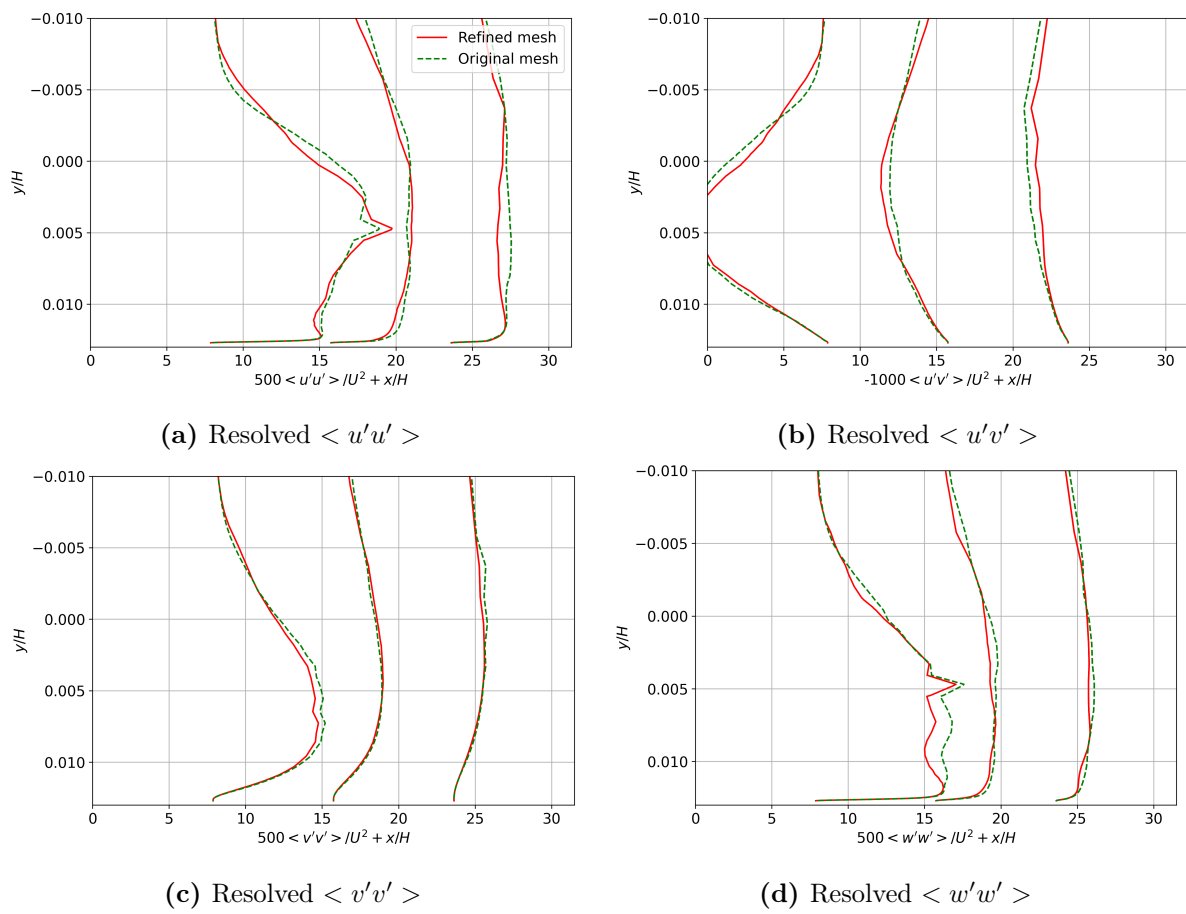
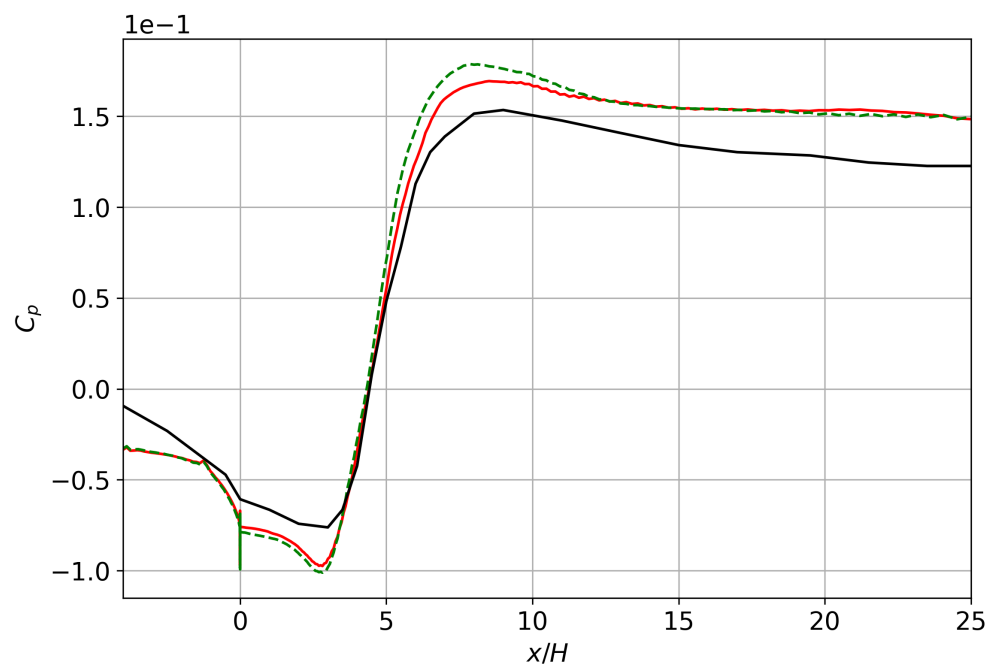**Figure 5.22:** Development of the turbulent stresses for the BFS downstream of the step.

Figure 5.23: Results for the pressure fluctuations for the BFS are shown.

5.3   FRPM-TAU: Aerodynamic test case

The difficulty of this test case was providing the FRPM patch with the required turbulence statistics and a quick solution was not found as mentioned in section 4.2.3. Since the FRPM patch is aligned with the global coordinate system, the capability of turning the entire CFD/CAA mesh must be provided by the CFD solver to be able to place the patch on a downward tilted surface (i.e., tilted relativ to the global coordinate system). However, this was achieved with the tools provided with TAU. However, due to the failure to achieve realistic synthetic turbulence this case was dropped (see 4.2.3).

5.4   FRPM vs. STG

In this section FRPM is compared with the STG. The best settings found for FRPM for the flat plate case, namely a patch length of 3δ, $lfac = 6$ and $\sigma = 2$, are compared to results obtained for the STG in section 5.4.1. Then FRPM is compared with its BFS setup to the STG in section 5.4.2.

5.4.1   Flat plate

FRPM coupled with TAU is compared to the volumetric forcing of the STG coupled with TAU over a length of $1/2\delta_0$ in terms of C_f in fig. 5.24. The pressure fluctuations are compared in fig. 5.25. A closer match with the Coles-Fernholz reference is achieved with the STG which has the Reynolds stresses of the precursor SA-RANS at the RANS-WMLES interface as a target. As opposed to the STG, FRPM has a target that changes over the length of the injection region.

It is notable that FRPM tries to match a target which is based on an underlying SST-RANS, although the SA-RANS model is applied in the tested HRLM setup. This may seem like a conflict, however, FRPM is seen as a black box providing synthetic turbulence which seeks to be as realistic as possible. In a first assumption, it is irrelevant how it is obtained. Of course, FRPM tries to reconstruct the TKE and this is directly provided by the SST. For more details on the STG analysis the reader is refered to [13].

In terms of spurious noise generation the well behaved aeroacoustic qualities of FRPM are seen in fig. 5.25. The spurious noise level for FRPM is negligible when compared to the STG. As is the case for C_f, FRPM with the eddy-relaxation term accomplishes a smoother introduction of the turbulence.

5.4.2   BFS

Fig. 5.26 shows the C_f for FRPM, the STG, experimental data and for the case of no injected synthetic turbulence. For the BFS, FRPM shows a closer match with the reference in the injection region while the STG results in much higher values for C_f and a marked peak directly at the step. Further, the STG shows a recirculation area that is slightly shifted upstream towards the step, and therefore shortening the reattachment region. With increasing distance from the step the STG shows a closer match with the experimental data than FRPM. Without synthetic turbulence there is an underestimation of C_f in the injection region and downstream of the step as expected, and the reattachment region is shifted downstream.

There is a diminishing effect from the synthetic turbulence downstream in the turbulent stresses as shown in fig. 5.27.
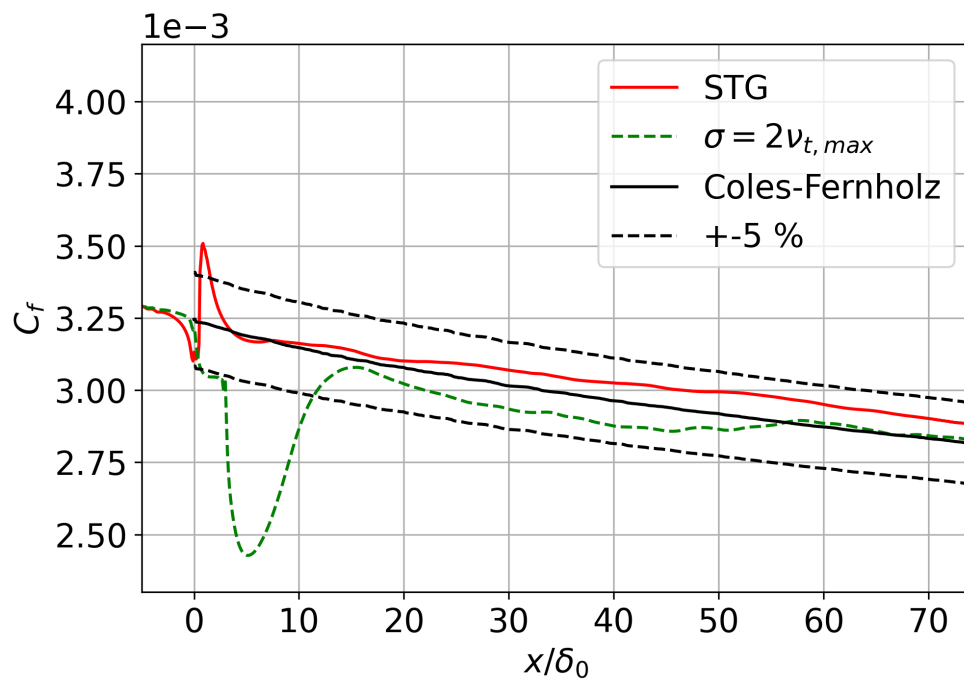
Figure 5.24: Results for C_f on the flat plate comparing the STG to a best practice FRPM setup. The STG solution data was kindly provided by Elrawy Soliman.
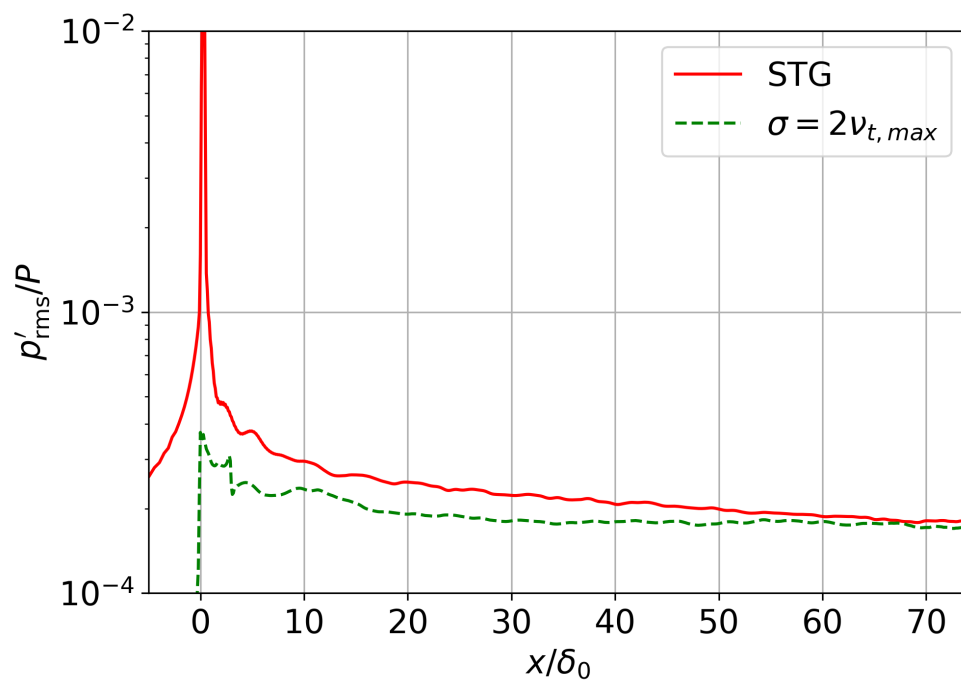

Figure 5.25: Results for the pressure fluctuations on the flat plate comparing the STG to a best practice FRPM setup. The STG solution data was kindly provided by Elrawy Soliman.
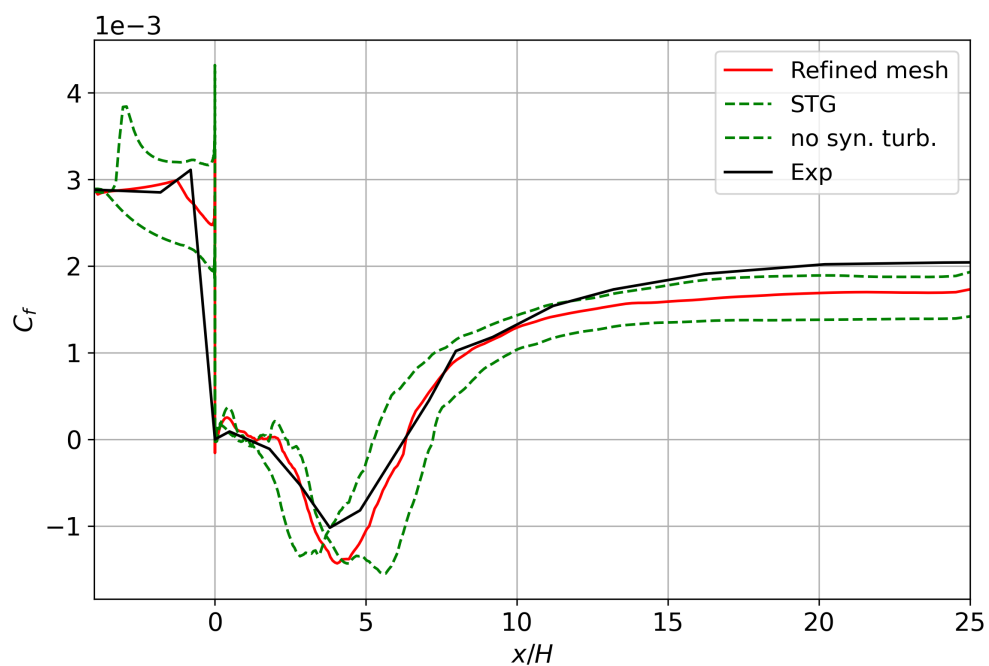
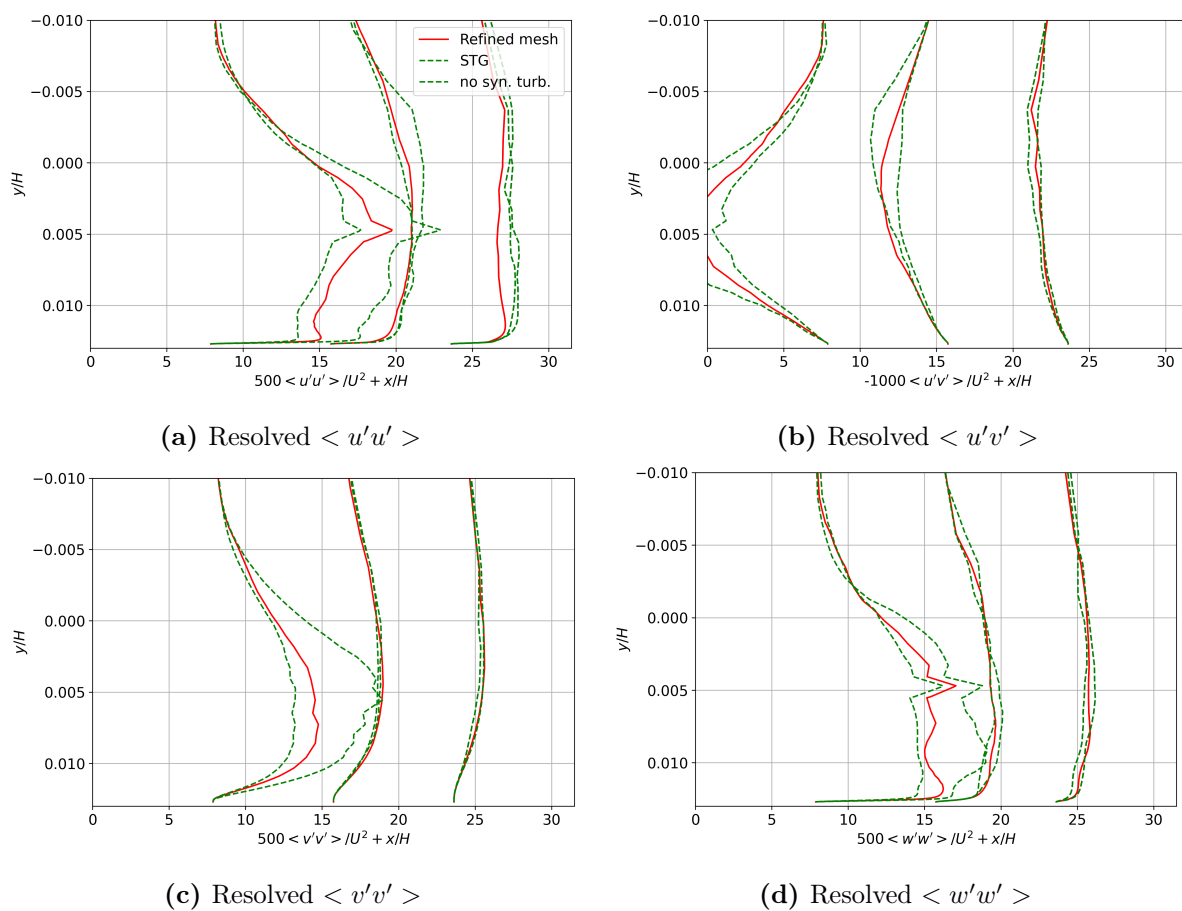**Figure 5.26:** Results for the skin friction for the BFS are shown.

(a) Resolved $< u'u' >$

(b) Resolved $< u'v' >$

(c) Resolved $< v'v' >$

(d) Resolved $< w'w' >$

Figure 5.27: Development of the turbulent stresses for the BFS downstream of the step.
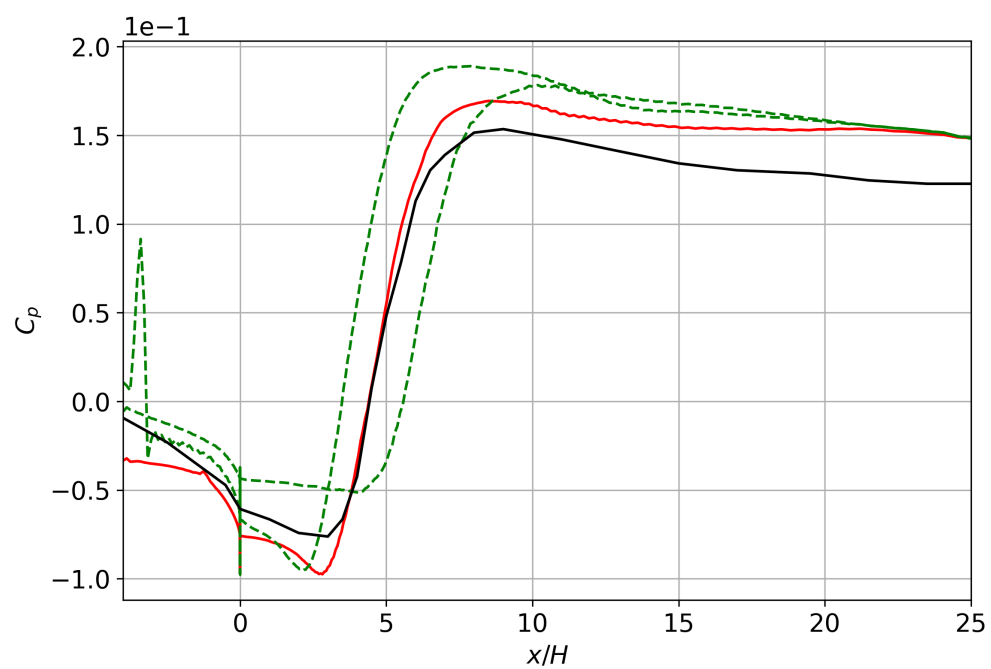
Figure 5.28: Results for the pressure fluctuations for the BFS are shown.

Chapter 6

Conclusions and outlook

The focus of this thesis was the integration of an optimized aeroacoustic turbulence generator, namely FRPM, into an embedded WMLES setup to investigate the suitability for aerodynamic applications. Current synthetic turbulence generators have a prolonged adaption region before establishing mature turbulence. The challenge is to inject more realistic turbulence, thereby shortening the adaption region.

A key part of the investigations was to implement coupling of FRPM with DLR-TAU and establish suitable settings for the coupling parameter σ. In both cases investigated, twice the maximal eddy viscosity worked well for obtaining values for C_f close to the reference value. The integral length scale of the synthetic turbulence was then varied to alter the size of the turbulent structures. In the flat plate test case, full recovery of Cf was observed when larger integral length scales were imposed. Smaller integral length scales led to lower turbulent stresses and no full recovery. For the backward facing step with strong natural instabilities, the small integral length scales of the injected FRPM turbulence improved the aerodynamic results in terms of the skin friction. For instance, the reattachment region behind the recirculation area of the experimental data was matched in its location. This was not the case for the aerodynamically optimized STG which generally led to an overprediction in the skin friction. As FRPM does not directly model any shear stress, and the BFS is known to also work without any turbulence injection, it can explain why the lower added turbulent intensities by the smaller structures help to reach the reference C_f levels. STGs developed specifically for the prediction of noise may be well suited for these kinds of flows with inherent instabilities because they smoothly blend in, while at the same time delivering turbulent content that can help to lessen the grey area problem. In case of FRPM, higher turbulent intensities may be needed for stable flows that rely on the injection as a source of turbulent content when transitioning from RANS modeling to resolved turbulence downstream. With an adaption region of roughly 10 δ_0, FRPM shows comparable results to STGs deliberately developed for the field of aerodynamics.

A limitation of FRPM is that in cases such as the flat plate it was demonstrated that a length of 3 δ_0 is optimal for the patch. This is quite restrictive for more complex geometries. Further, the restricition to cartesian, equidistant grids (for example curve linear meshes are prohibited) adds to this limitation. On the other hand, shorter FRPM patches may be sufficient in flows with strong instabilities as it is the case for the BFS, where an overall improvement of the results was seen when adding synthetic turbulence with FRPM.

Another limitation of FRPM is the absence of modeling for anisotropy and therefore shear stress. However, versions of FRPM modeling anisotropy exist and potential improvements can be expected for aerodynamic applications from such source terms.

Bibliography

[1] D Yu Adamian, Mikhail Khaimovich Strelets, and Andrei Konstantinivich Travin. An efficient method of synthetic turbulence generation at les inflow in zonal rans–les approaches to computation of turbulent flows. *Matematicheskoe modelirovanie*, 23(7):3–19, 2011.

[2] RAD Akkermans, Paul Bernicke, Roland Ewert, and Jürgen Dierke. Zonal overset-les with stochastic volume forcing. *International Journal of Heat and Fluid Flow*, 70:336–347, 2018.

[3] J.W. Delfs, R. Ewert, M. Bauer, and M. Siefert. *Stochastic Solenoidal Sources with the fRPM-Method.* GE Aircraft Engine, Brunswick, Germany, 2016.

[4] R. Ewert. Rpm-the fast random particle-mesh method to realize unsteady turbulent sound sources and velocity fields for caa applications. Technical Report AIAA Paper 2007-3506, 13th AIAA/CEAS Aeroacoustics Conference, 2007.

[5] Roland Ewert, Juergen Dierke, Andrej Neifeld, and Mohsen Alavi Moghadam. Linear-and non-linear perturbation equations with relaxation source terms for forced eddy simulation of aeroacoustic sound generation. In *20th AIAA/CEAS Aeroacoustics Conference*, page 3053, 2014.

[6] Marius Herr and Axel Probst. Effiziente modellierung der wandnahen turbulenz in hybriden rans-les simulationen. 2019.

[7] Doug McLean. *Understanding aerodynamics: arguing from the real physics.* John Wiley & Sons, 2012.

[8] Charles Mockett, Marian Fuchs, Andrey Garbaruk, Michael Shur, Philippe Spalart, Michael Strelets, Frank Thiele, and Andrey Travin. Two non-zonal approaches to accelerate rans to les transition of free shear layers in des. In *Progress in hybrid RANS-LES modelling*, pages 187–201. Springer, 2015.

[9] Axel Probst, Johannes Löwe, Silvia Reuß, Tobias Knopp, and Roland Kessler. Scale-resolving simulations with a low-dissipation low-dispersion second-order scheme for unstructured flow solvers. *AIAA Journal*, 54(10):2972–2987, 2016.

[10] Axel Probst and Philip Ströer. Comparative assessment of synthetic turbulence methods in an unstructured compressible flow solver. In *Progress in Hybrid RANS-LES Modelling*, pages 193–202. Springer, 2020.

[11] Mikhail L Shur, Philippe R Spalart, Mikhail Kh Strelets, and Andrey K Travin. A hybrid rans-les approach with delayed-des and wall-modelled les capabilities. *International journal of heat and fluid flow*, 29(6):1638–1649, 2008.

[12] M.L Shur, P. R. Spalart, M. K. Strelets, and A. K. Travin. Synthetic turbulence generators for rans-les interfaces in zonal simulations of aerodynamic and aeroacoustic problems. *Flow, Turbulence and Combustion*, 93(1):63–92, 2014.

[13] Elrawy Soliman. *Assessment and Improvement of Zonal Grey Area Mitigation Methods-*

Towards a faster RANS-to-LES transition. PhD thesis, Delft University of Technology, 2023.

[14] Philippe R Spalart. Comments on the feasibility of les for wings, and on a hybrid rans/les approach. In *Proceedings of first AFOSR international conference on DNS/LES*. Greyden Press, 1997.

[15] Philippe R Spalart. Philosophies and fallacies in turbulence modeling. *Progress in Aerospace Sciences*, 74:1–15, 2015.

[16] Jochen Wild, Michael Pott-Pollenske, and Bjorn Nagel. An integrated design approach for low noise exposing high-lift devices. In *3rd AIAA Flow Control Conference*, page 2843, 2006.

List of Figures